POLITECNICO DI TORINO

Master's Degree in Nanotechnologies for ICTs

Master's Degree Thesis

Design and optimization of a Lab-on-Chip for application in cardiac biomarkers detection

Supervisors

PhD Valentina BERTANA

Co-Supervisors

Prof. Matteo COCUZZA

PhD Simone Luigi MARASSO

Candidate

Giovanni NOTO

July 2024

Abstract

In recent years, many studies have focused on organic bioelectronics, an emerging technology that employs organic transistors for biosensing applications. Compared to their inorganic counterparts, organic transistors exhibit several advantages, such as biocompatibility, low cost, high sensitivity, flexible substrate compatibility, easy fabrication and low-temperature processability.
A specific category of organic transistors, the subject of this thesis, is the organic electrochemical transistor (OECT). In this device, the channel is typically made of a conductive polymer, such as Poly(3,4-ethylenedioxythiophene) polystyrene sulfonate (PEDOT:PSS), in contact with an electrolyte in which the gate is immersed. OECTs act as a transducer and amplifier of an ionic signal into an electrical one, operating at low voltages and providing significant amplification; this characteristic makes them highly pertinent in biosensing applications, such as medicine and biology.
The objective of this thesis is to fabricate and optimize a microfluidic platform which embeds both the OECT and the functionalized gate in the framework of the funded 'LIFEBLOOD' project. This platform was designed to detect the increase of two cardiac biomarkers, cardiac troponin (cTnI) and C-reactive protein (CRP), aiming to attain infarction early detection. Furthermore, a microfluidic blood/plasma separator (BPS) was designed to extract the plasma that will be used for the detection measurements. The integration of the OECT and BPS enables the creation of a Lab-on-Chip, which is the final objective of LIFEBLOOD project. OECT microfluidics and BPS were obtained by a combination of stereolithography and replication processes (soft-lithography), while gates and OECTs were fabricated using photolithography and inkjet printing. A variety of techniques and ink formulations were tested to optimize the printing process for PEDOT:PSS (which is the conductive polymer selected).
Subsequently, electrical characterizations were performed, which entailed the extraction of principal figures of merit and the analysis of the stability of the devices. At the end, the BPS demonstrated to allow deionized water flow and will be tested with blood. The fabricated OECTs showed a proper current modulation which is fundamental for final device sensitivity.

Table of Contents

Acronyms VI

List of Symbols IX

1 Introduction 1

2 Theoretical Background 3
2.1 Biosensors and Cardiac Biomarkers . . . 3
2.2 Organic Transistors . . . 10
2.3 Organic Semiconductors . . . 20
2.3.1 PEDOT:PSS . . . 21

3 Experimental 24
3.1 Fluidic sensing platform fabrication . . . 24
3.1.1 Objet 3D printer . . . 26
3.1.2 PDMS . . . 27
3.2 Biosensor fabrication . . . 30
3.3 PEDOT:PSS deposition . . . 34
3.3.1 Inkjet . . . 35
3.3.2 Aerosol jet . . . 42
3.3.3 Profilometer . . . 44
3.4 Measurement setup . . . 44
3.5 Microfluidic Blood/Plasma separator fabrication . . . 50

4 Results and Discussion 54
4.1 PEDOT:PSS ink formulation . . . 54
4.2 Measurements . . . 55
4.3 BPS test . . . 63

5 Conclusions and Perspectives 66

Bibliography 68

Acronyms

PDMS
Polydimethylsiloxane

EDOT
Ethylenedioxythiophene

PEDOT
Poly(3,4ethylenedioxythiophene)

PSS
Poly(styrene sulfonate)

PEDOT:PSS
Poly(3,4-ethylenedioxythiophene) polystyrene sulfonate

EG
Ethylene glycol

DBSA
Dodecylbenzenesulfonic acid

GOPS
(3-glycidyloxypropyl)trimethoxysilane

cTnI
Cardiac troponin

CRP
C-reactive protein

LOC

Lab-on-chip

POC

Point-of-Care

LOD

Limit of detection

BRE

Biorecognition element

EDL

Electric double layer

FET

Field-effect transistor

MOSFET

Metal oxide field-effect Transistor

ISFET

Ion-sensitive field-effect Transistor

RBC

Red blood cell

WBC

White blood cell

OECT

Organic electrochemical transistor

OFET

organic field-effect transistor

EGOFET

Electrolyte gated organic field effect transistor

OSC

Organic semi-conductor

OMIEC

Organic mixed electronic-ionic conductor

SRN

Signal-to-noise ratio

CAD

Computer-aided design

DMSO

Dimethyl sulfoxide

SMU

Source/Measure unit

BPS

Blood-Plasma separator

SLA

Stereolithography

List of Symbols

Sign	Description	Unit
I_{DS}	Drain current	A
I_{GS}	Gate current	A
V_{DS}	Drain voltage	V
V_{GS}	Gate voltage	V
R	Resistance	Ω
g_m	Transconductance	S
q	Elementary charge	C
μ	Carrier mobility	$m^2/V*s$
μ_{sat}	Saturation carrier mobility	$m^2/V*s$
μ_{lin}	Linear carrier mobility	$m^2/V*s$
V_{th}	Threshold voltage	V
V_p	Pinch-off voltage	V
C^*	Volumetric capacitance	F/m^2
C_{ch}	Channel capacitance	F/m^2
W	Width of the channel	m
L	Length of the channel	m
d	Film thickness	m
τ	Transit time (generic)	s

Chapter 1

Introduction

The activities reported in the present thesis fall within the project "A lab-on-chip integrated with electrochemical transistors for cardiac biomarkers evaluation in human blood (LIFEBLOOD)" (PIANO NAZIONALE DI RIPRESA E RESILIENZA (PNRR) Missione 4 - Componente 2 - Investimento 1.1 “Fondo per il Programma Nazionale della Ricerca (PNR) e Progetti di Ricerca di Rilevante Interesse Nazionale (PRIN)” - Finanziato dall’Unione europea – NextGenerationEU - Bando PRIN 2022), coordinated by *Università degli Studi di Napoli Federico II* with principal investigator *Valentina Preziosi*.
This thesis has been developed at *Chilab - Materials and Microsystems Laboratory of Chivasso* (TO) managed by the DISAT department of *Politecnico di Torino*.
The aim of this project is to create a portable and fast responding device (a better approach with respect to the electrocardiogram (ECG)) capable of detecting cardiac troponin (cTnI) and C-reactive protein (CRP), biomarkers indicating a myocardium problem and possible acute myocardial infarction (AMI). To achieve this, the idea is to create a Lab-On-Chip (LOC) essentially based on:

- a well-designed microfluidic device capable of separating blood cells and plasma, since the human blood is composed by different constituents and certain analyses require purification;
- OECTs, acting as biosensors, detect and monitor the biomarkers of interest. Detection is possible thanks to the gates’ functionalization with antibodies and aptamers, which are the recognition molecules to which the biomarkers bind.

By estimating the CRP-cTnI ratio it is possible to prevent, or early detect, the AMI since the CRP and CTnI rise sharply within a few hours of the acute phase triggering event. LOC implements several functions in a single device and, in this case, can replace the traditional blood analysis, as it offers many advantages in

terms of volume of biological fluid required, cost, size (and therefore portability), speed of analysis (real-time) and efficiency.
Concerning the OECT, they are nowadays very investigated especially for the biomedical and sensing applications, due to their improved biological and mechanical compatibility with tissues [1]. OECTs are a subset of organic transistors, an evolution of the classical silicon-based transistors, where the channel between source and drain is made of organic semiconductor material (one of the most common is PEDOT:PSS). In OECTs, the channel is in contact with an electrolyte in which the gate electrode is immersed. These devices can achieve a very high gate-channel capacitances and can therefore operate at very low voltages (<1 V), allowing the detection of cells, biomolecules or other species without affecting or degrading them.
An important figure of merit of OECT is transconductance, which is defined as the ratio of the change in current I_{DS} at the output terminal to the change in voltage V_{GS} at the input terminal of an active device ($g_m = \frac{\delta I_{DS}}{\delta V_{GS}}$) [2].
Transconductance measures the device's ability to amplify an input signal by evaluating the change in drain current (I_{DS}) with the variation of the gate voltage (V_{GS}) [3].
OECTs have a very high transconductance, which translates into a high sensing capability, as a small change in the gate voltage results in a large change in the channel current, enabling high resolutions and lower limit of detection, thus improving sensitivity [2].
Finally, OECTs use organic semiconducting materials that are flexible, biocompatible and low-cost [2].
This thesis focuses on the design and fabrication of OECT microfluidic integration and could be resumed in the following main steps:

- design and fabrication of fluidic and its holder;
- design and fabrication of OECT;
- deposition of PEDOT:PSS, the organic semiconductor selected and optimized;
- biosensor characterization;
- design and fabrication of microfluidic blood/plasma separator.

Following this introductory part, with the presentation and the objective of the work, the theoretical background has been presented, in particular regarding the OECT and the organic semiconductors. In the following two chapters the experimental and results part is discussed with different setups, instruments and measurements.

Chapter 2

Theoretical Background

2.1 Biosensors and Cardiac Biomarkers

Detection of biomolecules and biomarkers is a crucial aspect of clinical diagnosis. Consequently, recent research has focused on the development of biosensors with high performance, evaluated in terms of sensitivity, selectivity, limit of detection (LOD), dynamic range, resolution, response time, stability, life cycle (reusability). The International Union of Pure and Applied Chemistry (IUPAC) defines a biosensor as: "A device that uses specific biochemical reactions mediated by isolated enzymes, immune systems, tissues, organelles or whole cells to detect chemical compounds usually by electrical, thermal or optical signals" [4].

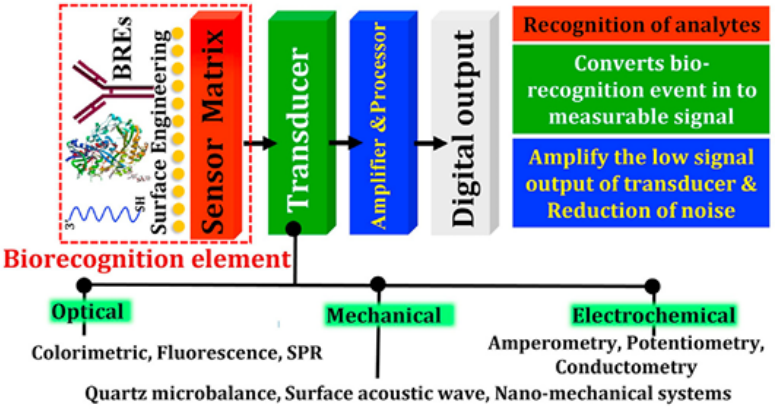

Figure 2.1: Biosensor scheme, with function of each part and transducer classification [4]

Evaluating a biosensor involves the extraction of the previously cited analytical parameters from the "output signal vs concentration" calibration plot, shown below:

- Sensitivity, corresponds to the slope of the calibration plot and indicates the change in the output signal due to a change in the analyte concentration;
- Selectivity, is the ability of differentiation, by which the biosensor responds selectivively to a target molecule;
- Limit of Detection (LOD), is the lowest concentration that can be distinguished, and in general it is expressed as: $LOD = 3 * \frac{SD_{blank}}{Slope}$, where SD_{blank} is the standard deviation of blank and slope is the sensitivity;
- Dynamic range, is the concentration range between the detection limit and the upper limiting concentration;
- Linearity, is the relative deviation from an ideal straight line of the calibration plot;
- Limit of Quantification (LOQ), corresponds to the minimum concentration at which qualitative results can be achieved with a high degree of confidence, and in general is equal to: $LOQ = 10 * \frac{SD_{blank}}{Slope}$, where SD_{blank} is the standard deviation of blank and slope is the sensitivity;
- Resolution, is the lowest concentration difference that can be detected;
- Response time, is the time for a sensor to generate a signal in response to a change in concentration of the analyte;
- Stability, is the ability of the sensor to maintain its performance over the time;
- Life cycle, the total working time of the sensor.

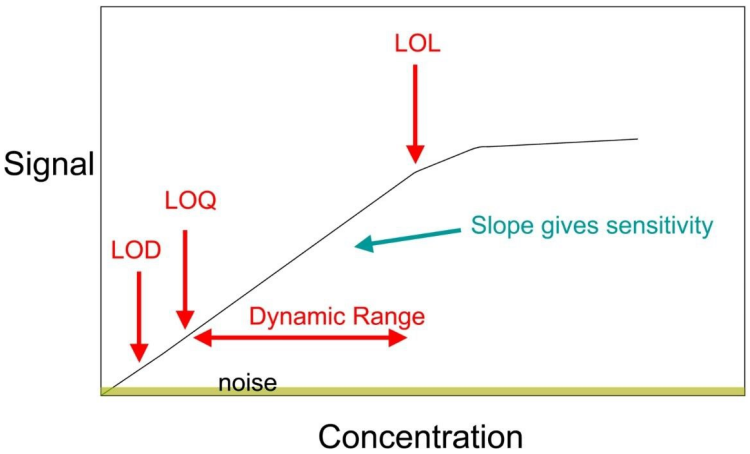

Figure 2.2: Calibration plot [5]

A biosensor is based on three main components:

- a biorecognition element (BRE), which is responsible for detecting the analyte under investigation;
- a transducer, which converts the biorecognition event into a measurable signal;
- a read-out, which displays the signal.

The majority of diffused BREs are antibodies, aptamers, enzymes, nucleic acids and molecular imprinted polymers (MIPs), reported in the successive figure.
One of the most important aspects in a biosensor is the immobilization of the BRE on the transducer, which must confine the biologically active material without damaging it.

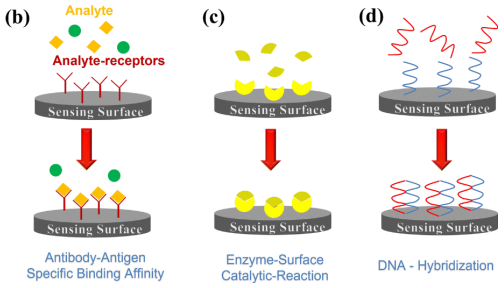

Figure 2.3: Binding with different types of BRE [6]

There are two possible immobilization mechanisms (shown in figure 2.4):

1. Binding, where the active material attaches directly to the surface of the transducer. It may be classified into two further categories:
   - adsorption, that is cheap and "gentle method", but the bonds formed are relatively weak;
   - covalent bonding, where the surface is treated to create reactive groups that result in stronger bonds.
2. Physical Retention, in which the active material is separated from the analyte by a semipermeable layer. This is further divided into two subcategories:
   - membrane confinement, based on a semipermeable membrane with pores that are large enough to permit the analyte and the solution to diffuse through, while retaining the active material within the membrane;
   - matrix entrapment, based on a porous encapsulation matrix around the active material, which allows the analyte and the solution to diffuse through.

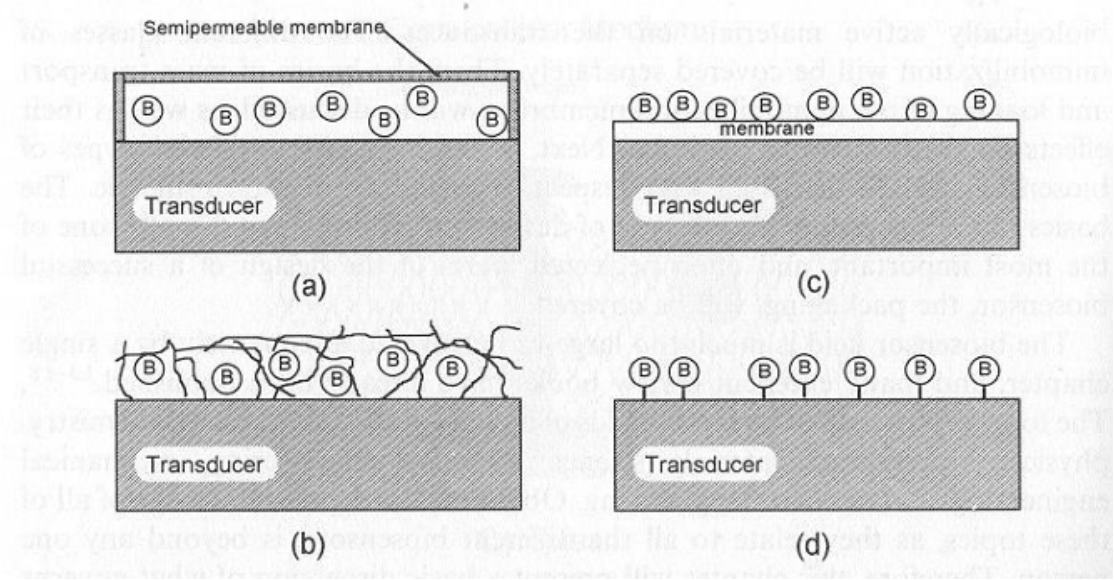

Figure 2.4: Immobilization mechanisms of biologically active material "B": (a) membrane confinement, (b) matrix entrapment, (c) adsorption, (d) covalent bonding [7].

The configuration of biosensor may vary depending on the transducers and the signal obtained, which is displayed as a digital output. In fact, biosensors can be classified into: optical, mechanical/piezoelectric, thermal, electrochemical, etc.[8] In optical biosensors the binding event changes a property (like phase, polarization, or frequency) of light, proportionally to the concentration of the absorbed analyte [9]; thermal biosensors feel the change in temperature during the reaction; mechanical biosensors detect changes in mass, forces, motion after the biomolecular interaction (like piezoelectric effect), and in general they are based on a vibrating element, such as cantilever or quartz crystal microbalances (QCM). Electrochemical biosensors instead evaluate the changes in current, potential and conductance that occur when the target molecule interacts with the BRE. Depending on what it measures, electrochemical biosensors can be classified into:

1. Voltametric, in which a potential is applied to a reference electrode, leading to a redox reaction of the electrolytes in the solution, so the resulting current is measured and expresses the reaction rate; in fact, the current response is proportional to the analyte concentration. It is possible to apply different voltage patterns for obtaining different biosensor configurations, like for example the amperometric biosensor in the case of constant voltage, or cyclic voltammetry biosensors in the case of triangular wave [8].
   One of the most common reference electrodes, by which it is possible to apply

a known bias, is Ag/AgCl, able to compensate the potential drop at the electrode-electrolyte interface (EDL effect), based on the following reaction:
$Ag^+ + e^- \leftrightarrow Ag(s)$
$AgCl(s) + e^- \leftrightarrow Ag(s) + Cl^-$

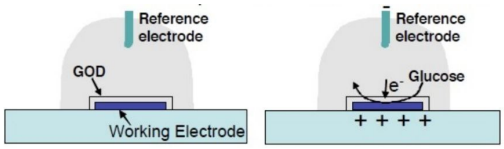

Figure 2.5: Amperometric biosensor (for glucose) [5]

2. Conductometric, in which it is possible to measure the change in conductivity (or resistivity) that depends on the concentration of all ions. The electrical impedance is measured between two electrodes, the working and the counter, dipped in the solution.

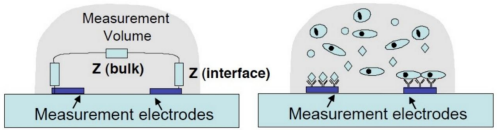

Figure 2.6: Conductometric biosensor [5]

3. Potentiometric, in which a potential is obtained by measuring the potential difference between a reference and a working electrode; an accumulation of charge is obtained due to the binding of the target on the electrode surface. The relation between concentration and potential is dictated by Nernst Equation:
$E_{cell} = E^0_{cell} - \frac{RT}{nF} lnQ$
where E_{cell} is the potential of the electrochemical cell in zero current, E^0_{cell} is the constant potential of the electrochemical cell, R is the real gas constant, T is the absolute temperature, n is the number of electron transfer, F is the Faraday constant, and Q is the ratio of ion concentrations at the reduced state and oxidized state [4]. In general, potentiometric biosensors can be divided into ion-selective electrodes (ISEs), coated wire electrodes (CWES), and field-effect transistors (FETs). One of the most common electrical sensing structures is based on three stacked layers, metal, insulator and semiconductor, with three terminals (MOSFET). An evolution of this potentiometric biosensor is the ISFET (ion-sensitive field-effect transistor), which offers different advantages, especially in terms of mass production.

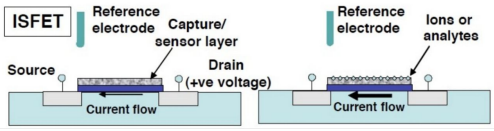

Figure 2.7: Potentiometric biosensor (ISFET) [5]

Biosensors are nowadays very integrated in wearable devices or in LOC, enabling the rapid detection of analytes using a minimal sample volume, such as the blood-plasma separation platform under analysis. Indeed, blood represents the most prevalent fluid utilized in microfluidic channels and biosensors. Blood is a fluid based on a suspension of cells, including red blood cells (RBCs), which are deformable cells that impact on physiological flow, white blood cells (WBCs), and platelets, immersed in a low-viscosity fluid called plasma. Plasma is a water solution composed of cations, anions and other substances (like proteins) which have a strong impact on the electrical response of blood [10]. The aim of this platform is to separate and extract plasma from blood (removing the corpuscular part), in order to evaluate the presence and the concentration of cTnI and CRP. These two proteins are cardiac biomarkers; cardiac-troponin (cTnI) is usually detectable 2-4 hours after the infarction, whereas c-reactive protein (CRP) is always present in plasma, but its level increases during acute or chronic inflammation.
The inflammatory process comprises four components:

- inflammatory inducers;
- sensors, such as macrophages, and dendritic cells, which stimulate the production of chemical mediators in response to inducers;
- mediators, such as cytokines, which are cell-to-cell messengers;
- target tissues.

The inflammatory response starts within a few minutes and may persist for several days, until the inflammation has been eliminated and the tissue has been repaired. Particular attention is focused on investigating the correlation between the onset of different pathologies and inflammation-related biomarkers, such as acute-phase proteins [9].
Biomarker is defined as a biomolecule that plays a pivotal role in different biological and pathological processes or gives a specific pharmacological response to a drug [11].
Due to its complex structure and the need for high performance during the recognition of biomarkers, especially in terms of selectivity and sensitivity, nanotechnology is being investigated for the development of biosensors.

Biomarkers can be classified into exposure biomarkers and disease biomarkers. Exposure biomarkers are used to predict a disease, whereas disease biomarkers are used in monitoring, screening, and diagnosis of disease.
Human plasma is the most important source of circulating biomarkers, but its extraction is typically performed by centrifugation [12]; this mechanism requires large equipment also for a small volume of sample, so the development of a POC device is investigated for plasma separation (first platform).
The concentration of the two cardiac biomarkers is measured in a second platform responsible for the in-situ detection of the target by functionalized OECT.
The objective of this project is to optimize and integrate the two aforementioned platforms into a final LOC platform, as illustrated in the following figure.

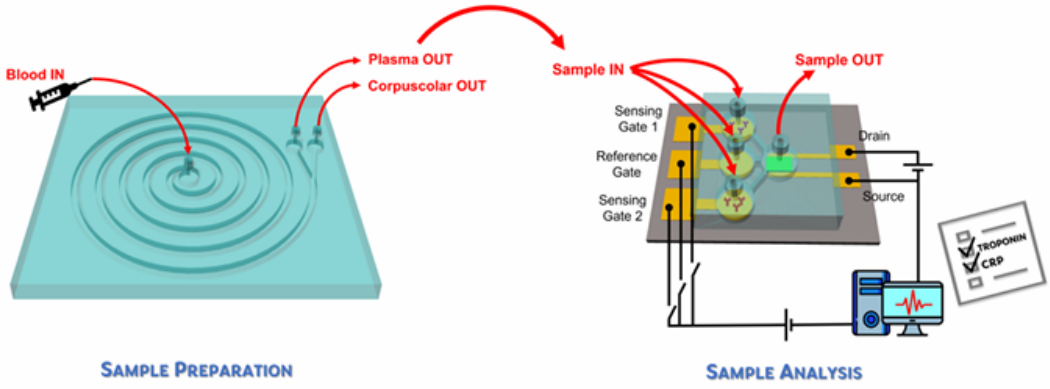

Figure 2.8: LOC platform scheme [13]

2.2 Organic Transistors

The advent of modern semiconductor technology has led to a significant increase in the use of transistors as switches and amplifiers in any electronic circuit.
A transistor is a device that has the ability to control, amplify, and modulate electrical signals and consists of three electrical terminals called source, drain and gate.
Transistors are based on field-effect doping, which modulates the number of mobile carriers inside a semiconductor by applying a voltage to a metallic electrode, which is separated from the semiconductor by a thin insulating layer [14]; for this reason, FETs are defined as voltage-controlled.
Recent research has demonstrated the potential of organic semiconductors, which offer a cost-effective alternative to silicon, due to their amenability to deposition and patterning at ambient temperature, since individual layers in organic FET can be deposited and patterned using direct writing techniques.
As regard charge carriers, traditional inorganic semiconductors exhibit a high density of charge carriers in the bulk, generated thermally due to doping; in contrast, undoped organic semiconductors require the injection of charge carriers by the electrodes [15].
In a FET, when a voltage is applied between the gate and the channel, charge is accumulated near the interface with the dielectric (field-effect doping), leading to the formation of a parallel plate capacitor with a charge equal to Q = CV, where C is the capacitance of the dielectric and V is the gate voltage. It can be observed that capacitance is inversely proportional to the distance between the two plates; therefore, thin dielectric layers result in the greatest amount of induced charge and thus the greatest drain current of the transistor.

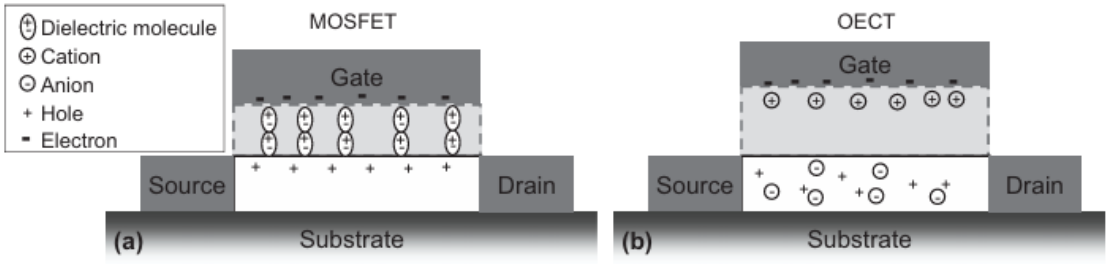

Figure 2.9: MOSFET vs. OECT [16]

Organic transistors can be divided into two categories: Organic Field-Effect Transistors (OFETs) and Organic Electrochemical Transistors (OECTs).
OFETs exhibit characteristics similar to those of inorganic field-effect transistors,

with the notable distinction that the semiconductor material is organic and the thin semiconductor layer is separated from the gate electrode by a thin insulating gate dielectric.
In OECTs, the organic semiconductor channel is in contact with an electrolyte in which the gate electrode is immersed. The operation of an OECT is based on the injection of ions into the organic film through the electrolyte, which changes the doping state of the film and therefore its conductivity, leading to a very high transconductance [2].
The peculiarity of OECTs is that doping occurs throughout the entire volume of the channel, in contrast to a thin interfacial region in field-effect transistors, which leads to a volumetric capacitance. In fact, OECTs achieve gate-channel capacitance up to 9 $mFcm^{-2}$, which is more than three orders of magnitude greater than that observed in state-of-the-art high-k dielectrics. This large capacitance provides excellent amplification and allows the OECT to operate at low voltages (approximately 0.5/0.6 V) [2].
Another classification can be derived from how ions interact with the OSC; in particular, there are organic electrochemical transistors (OECTs) and electrolyte gated organic field effect transistors (EGOFETs).
In the former case, the OSC is permeable to ions, allowing for the control of charge carrier density in the device channel through electrochemical doping and de-doping; this classification is that of an organic mixed electronic-ionic conductor (OMIEC).
In the latter case, the OSC is not permeable to ions, resulting in the formation of an EDL is formed at the semiconductor/electrolyte interface; this causes a voltage drop, which in turn controls the charge carrier density [17].

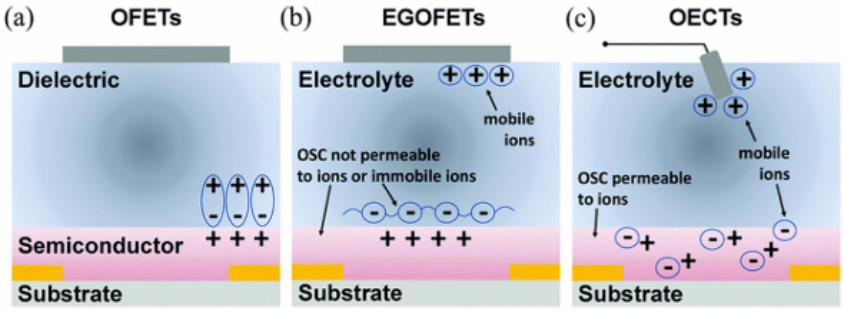

Figure 2.10: OFET vs EGOFET vs OECT [3]

Similarly, in OFET, as in the case of inorganic materials, gradual channel approximation can be employed to express the drain current as: $I_{DS} = \mu C_i \frac{W}{L}((V_{GS} - V_{th})V_{DS} - \frac{1}{2}V_{DS}^2)$, where C_i is the capacitance per unit area of the gate dielectric, and V_{th} the threshold voltage of the device.
Two regimes can be observed depending if $|V_{DS}| << |V_{GS}| - |V_{th}|$ or $|V_{DS}| >$

$|V_{GS}| - |V_{th}|$ (in both cases $|V_{GS}| > |V_{th}|$).
In the former case, the equation can be simplified as: $I_{DS} = \mu_{lin} C_i \frac{W}{L}(V_{GS} - V_{th})V_{DS}$, showing a linear behaviour, while in the latter case, which is known as the saturation regime, a depletion region arises at the interface between the organic semiconductor and the drain electrode, the channel is in pinch-off and the current becomes independent of the drain voltage: $I_{DS} = \frac{1}{2}\mu_{sat} C_i \frac{W}{L}(V_{GS} - V_{th})^2$ [17].
Organic bioelectronics refer to electronic devices that interface living systems through organic electronic materials in order to detect diseases by analyzing cells, tissues, and organs. OECTs can operate in aqueous environments and with microfluidic systems, making them an attractive option for sensing applications, particularly biosensing. This is due to their high transconductance, which enables them to reach a very low limit of detection. Furthermore, OECT fabrication is straightforward, low-cost and biocompatible with different substrates.
OECTs have two functions:

- switch, with V_{GS} as input and I_{DS} as output;
- amplifier, amplifying the input signal.

OECTs convert ionic fluxes, which are also amplified, into electronic signals. OECTs are V_{GS}-drive devices, so V_{GS} drives ions from the electrolyte into the permeable polymer, modulating its conductivity by de-doping and thus affecting the current flow (I_{DS}) [9].
I_{DS} is proportional to the number of electrons or holes for an n-type or p-type semiconductor, respectively, and their speed.
In standard operation, the gate and drain voltages are applied with respect to the source electrode, which is grounded. The obtained channel current corresponds to the output current of the OECT and its modulation is caused by the interaction between electronic and ionic charge carriers.

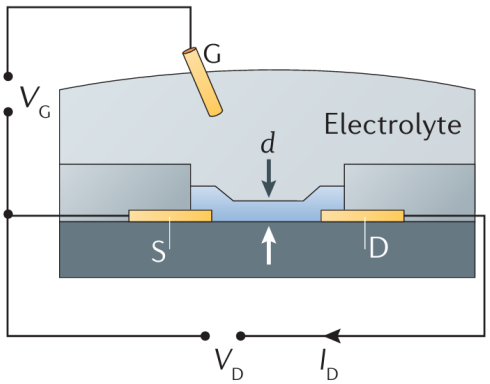

Figure 2.11: OECT representation [14]

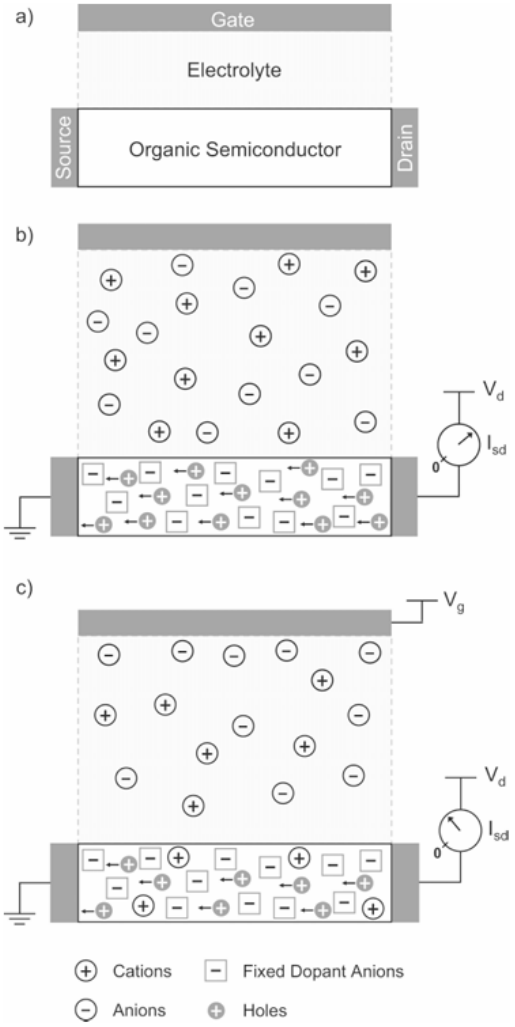

Figure 2.12: a) Another representation of OECT. b) OECT without gate voltage applied. c) OECT with gate voltage applied and current depends on de-doping effect [18].

OECTs have two possible operational modes, represented in the figure 2.13 and 2.14: depletion and accumulation, which depend on the intrinsic doping state of the channel material.
If the channel is made of an undoped polymer, the device operates in enhancement mode, going from OFF state to ON state when a voltage is applied, while, in the case of a conducting (doped) channel polymer, the device operates in depletion mode, so going from ON state to OFF state when a voltage is applied [19]. In the case of depletion mode, the channel is typically constructed using PEDOT:PSS (which will be discussed in the following paragraph).

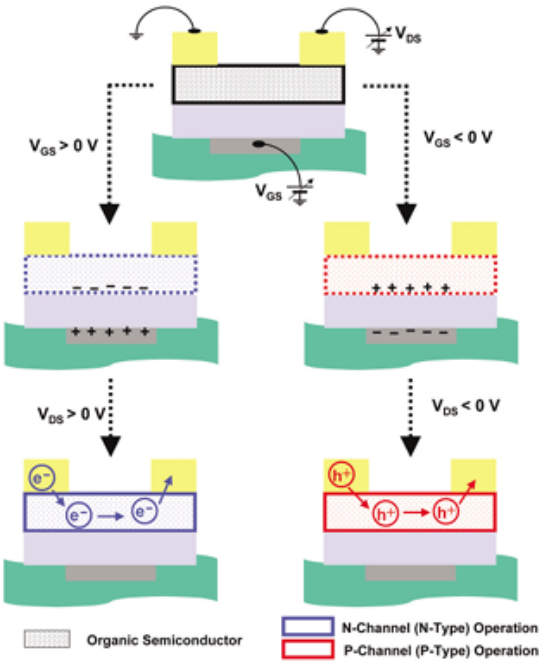

Figure 2.13: n-type and p-type channel transistors [20]

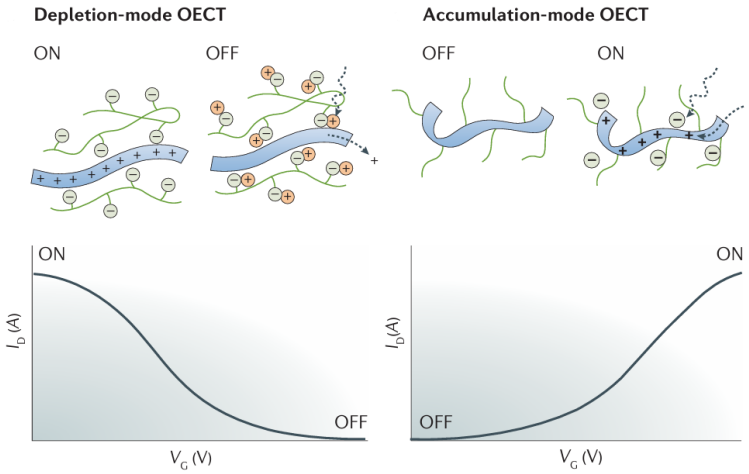

Figure 2.14: Operation modes of OECT [14]

Bernards and Malliaras develop a model to analyze the behaviour of an OECT and predict its transconductance and response time. This model considers the channel as the conjunction of an electronic circuit, which corresponds to a variable resistor, and an ionic circuit, based on a capacitor (representing the storage of ions) and a resistor (representing the flow of ions) in series, as represented in figure 2.15.

The electronic circuit corresponds to the conductivity of the channel and it is described by using Ohm's law:
$J(x) = q\mu p(x)\frac{dV(x)}{dx}$, where J is the current flux, q is elementary charge, μ is the hole mobility, p is the hole density and $\frac{dV(x)}{dx}$ is the electric field.
This is analogous to the silicon transistors, but in this case it can be achieved at room temperature and faster [18].

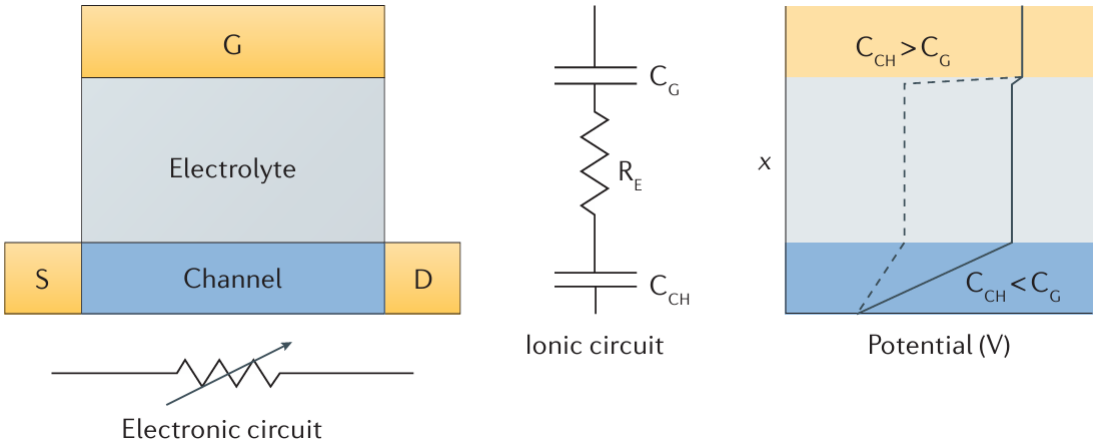

Figure 2.15: Electronic and ionic circuit representation, with on the right the distribution of potential. The solid line corresponds to the case of efficient gating, with voltage drops in correspondence of electrolyte–channel interface, while dashed line corresponds to the case of poor gating, where most of the applied gate voltage drops at the gate–electrolyte interface [14].

The model provides a good approximation of the steady-state of OECTs at saturation conditions. The OECT steady-state performance is evaluated by plotting the output and transfer characteristics, from which it is possible to extract some figures of merit, such as:

- pinch-off voltage V_p, which is the voltage at which the transistor switches from linear to saturation regime;
- threshold voltage V_{th};
- ON/OFF ratio; a larger ratio indicates a greater signal-to-noise (SNR) ratio, which also improves the limit of detection in the case of biosensors;
- transconductance g_m.

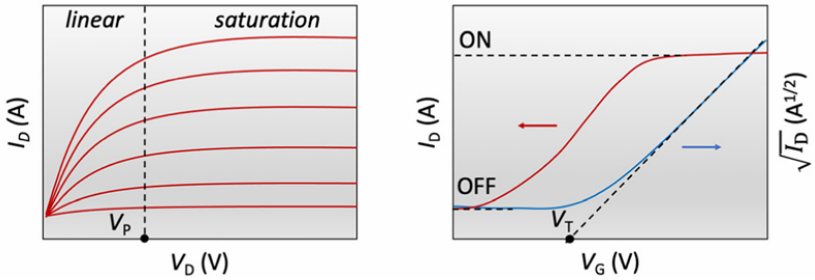

Figure 2.16: Examples of steady-state figures of merit, like pinch-off voltage in the output characteristic on the left, and threshold voltage in the transcharacteristic on the right [19].

In fact, the model allows for the prediction of the g_m as: $g_m = \frac{Wd}{L}\mu C^* |V_{th} - V_{GS}|$, where W is the width of the channel, d is the film thickness, L is the length of the channel, μ is the carrier mobility, C* is the volumetric capacitance, V_{th} is the threshold voltage, and V_{GS} is the gate voltage.
The only difference between this equation and the one for FETs is that here the thickness of the channel affects the performance, whereas in FETs equations' only capacitance per unit area (C') is considered. This implies that the transconductance depends on the geometry of the device, thereby offering the possibility to enhance the performance by modifying the channel ratio and biasing conditions. The subsequent equation normalizes the gm with the device geometry: $g_m(NR) = \frac{g_m L}{Wd}$.
The time required to switch ON or OFF an OECT is longer than that required for a FET, which operates at frequencies up to MHz range, while the OECT remains within the 10–100 kHz range. The response time is limited by either the electronic or the ionic circuit; in the case of PEDOT:PSS, the speed-limiting process is often the ionic charge transport, since hole transport is relatively faster. The response time of the OECT is dependent on the capacitance, which increases with film thickness; however, this can be optimized through a trade-off between the gain and the bandwidth.
Assuming a uniform doping, Bernard's model demonstrates that the drain current response to a square gate voltage pulse has an exponential time dependence:
$I_D(t) = I_{SS}(V_{GS}) + \Delta I_{SS}(1 - f\frac{\tau_e}{\tau_{on}})\exp(-\frac{t}{\tau_{on}})$, where $I_{SS}(V_{GS})$ is the steady-state channel current at the applied V_{GS}, ΔI_{SS} is the difference between the initial and final steady state currents (i.e., $I_{ON} - I_{OFF}$), f is a weighting factor corresponding to the gate current contribution to drain current and has a characteristic range from 0 to $\frac{1}{2}$, τ_e is the transit time of electronic charges in the channel, and τ_{on} corresponds to the RC time constant. In addition, $\tau_{on} = R_s C_{ch}$, where R_s is the electrolyte resistance, proportional to $1/\sqrt{WL}$, and C_{ch} is the channel capacitance, which scales linearly with the channel volume.
Another method for estimating τ_{on} is the impedance matching method, based on

the cutoff frequency (f_c), which corresponds to the frequency of the g_m at 3 dB, and is calculated using the following equation: $\tau_{on} = \frac{1}{2\pi f_c}$. Some strategies have been studied to decrease the OECT response time and given the relationship between channel geometry and g_m, L should be as small as possible to maximize g_m, while W and d could change depending on the application [19].
The electronic transit time is described by $\tau_e = \frac{L^2}{\mu V_{DS}}$. It should be noted that upon removal of the applied gate current, there is a slow recovery of the source-drain current, due to the diffusion of cations from the semiconductor back into the electrolyte.

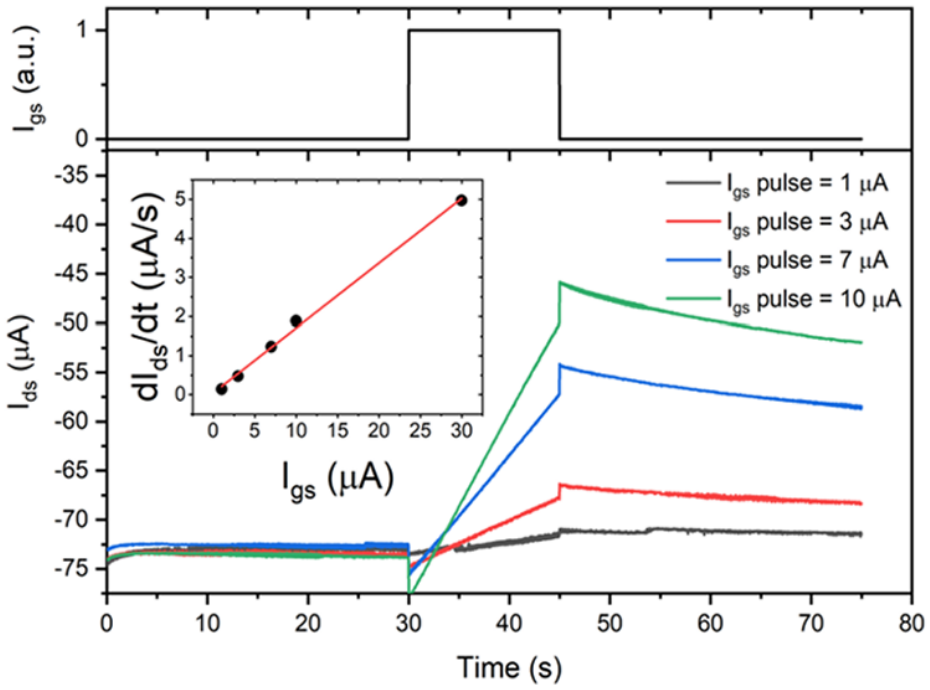

Figure 2.17: Example of time of flight measurement. A gate current pulse of 15 seconds is applied, with V_{DS} = -0.1 V. The inset shows the linear fit of $\frac{\delta I_{DS}}{\delta t}$ vs I_{GS} from which the hole mobility μ can be extracted [21].

Two possible approaches to steady-state can occur when a voltage is applied:

- monotonic decay ($\tau_i > f\tau_e$), where the sufficiently fast electronic response of the organic film can be ignored in the overall transit time;
- spike-and-recovery ($\tau_i < f\tau_e$), where the transient current is dominated by hole extraction from the film, since the hole transport is relatively slow.

The characteristic time constant for ionic transport in the electrolyte (τ_i) is determined by the solution resistance and capacitance of the ionic double layer.

Using Gouy–Chapman theory $\tau_i \sim \frac{l}{\sqrt{C}}$, where l is the distance between the organic film and gate electrode and C is the ionic concentration. Consequently, by reducing the distance between the gate electrode and the channel or by the increasing electrolyte concentrations, the response time can be enhanced.
The ratio between the transient time of electronic charges and that of ions allows the transient response to be optimized by changing the electrode location, the length of the organic film or the drain voltage [18].
In biosensing, it is crucial to minimize V_{GS} in order to achieve maximum transconductance at, or very close to, zero gate voltage. The gate voltage at which the maximum transconductance is reached, $V_{GS}(g_{m,max})$, exhibits a strong dependence on $\frac{W}{L}$. By varying the aspect ratio of the channel, while maintaining a constant channel thickness, it can be observed that a larger $\frac{W}{L}$ results in a higher maximum transconductance and ON current, but concurrently, a higher $V_{GS}(g_{m,max})$ is observed.
Instead, regarding the thickness of the channel, a thicker one is associated with both higher $g_{m,max}$ and $V_{GS}(g_{m,max})$ values.
Another method for varying $V_{GS}(g_{m,max})$is to change the gate electrode material; in fact, the Ag/AgCl electrode is more effective for turning OFF the transistor, while a polarizable electrode necessitates a larger gate bias to achieve the same result.
Finally, the maximum transconductance decreases significantly with the decrease in the drain voltage [22].
The fraction of the applied gate voltage that drops across the channel is controlled by the type and geometry of the gate electrode [14].
The gate can be classified as:

- polarizable, such as Au or Pt. In this case, the ionic circuit has two capacitors in series, one due to the formation of EDL and the other for the volumetric capacitance of the channel. The applied gate voltage drops across the smaller capacitor, as they are in series.

- non-polarizable, such as Ag/AgCl. In this case, the voltage drop at the gate/electrolyte interface is negligible.

In order to achieve effective gating, the capacitance of the gate electrode must be at least ten times larger than that of the channel, otherwise a large fraction of the applied gate voltage will drop at the gate electrolyte interface [14]; for this reason it is necessary to use a large-area gate in the case of a polarizable gate electrode.
Metals, such as gold and platinum, are the most commonly used materials for gate electrodes due to their high stability, high conductivity and ease of functionalization. For the same reason, source and drain electrodes are typically made with gold.

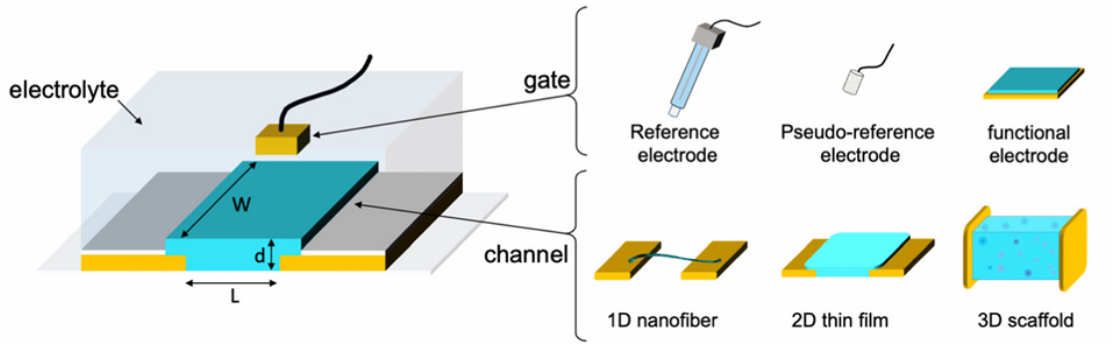

Figure 2.18: OECT scheme with different gates and different channel configurations [19]

The electrolyte employed in OECTs establishes a contact between the channel and the gate electrode and in general contains salt ions in the form of a liquid or a more complex biological fluid.
As regard the gate electrode, it can be placed on the same plane of the channel (planar) or immersed perpendicularly with respect to the channel; these different positions allow for various architectures (shown in the figure below), each with its own advantages and drawbacks. The majority of devices are manufactured in bottom contact configurations, as this allows for faster switching speed, while the top contact configurations improve the reproducibility, although parasitic reactions can occur at the electrolyte interface [19].

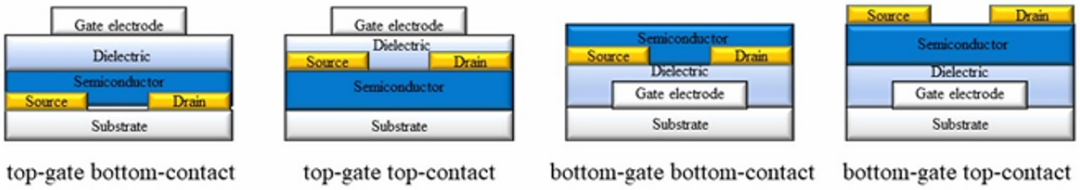

Figure 2.19: OECT configurations depending on the gate position [3]

In recent years, organic semiconductors have been employed to connect electronics with biological systems, as they can sustain both ionic and electronic transport [17]. The majority of organic semiconductors are p-type, and in particular more than 90% of the reported OECT-based biosensors employ PEDOT:PSS due to the following characteristics [2]:

- ease of use,
- robustness,

- biocompatibility,
- high transconductance,
- high stability,
- functionalization in a wide temperature range,
- low cost.

2.3 Organic Semiconductors

The principal advantage of employing organic semiconductor material, instead of silicon, in a FET is the reduced cost of fabrication, since it is possible to operate at ambient temperature and direct-printing techniques are used [15].
The term organic semiconductors refers to a class of materials that are predominantly composed of carbon and hydrogen atoms, with the addition of a few others elements. The conductivity of organic semiconductors is extrinsic and arises from the injection of charges at electrodes through doping and/or dissociation of electron-hole pairs [15].
Organic semiconductors can be classified into [15]:

- Amorphous molecular films, corresponding to organic molecules deposited through evaporation or spin-coating;
- Molecular crystals, formed by Van-der-Waals interactions;
- Polymer films, which consist on a chain of molecular repeated units, called monomer. The backbone of a semiconducting polymer is formed by a chain of carbon atoms with alternating single and double bonds. Many semiconducting polymers contain side chains that render them soluble in common organic solvents. They are processed in solution, which allows different deposition techniques including spin-coating and ink-jet deposition.

Conjugated polymers (CPs) are organic macromolecules able to combine the mechanical features of plastics with the electrical conductivity properties typical of metals. This is achieved through the alternation of σ and π bonds along their backbone.
σ bonds occur when the overlap of two molecular orbitals is along the principal axes (between the two nuclei), while π bonds occur when the overlap is perpendicular to the principal axes (above and below).

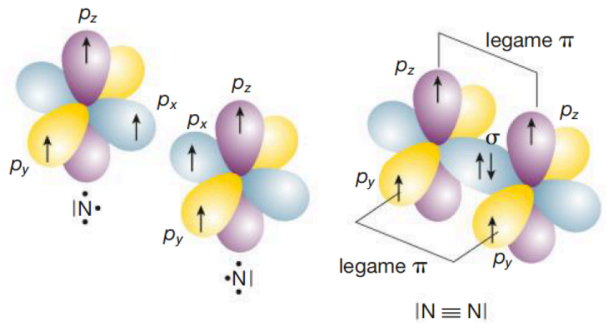

Figure 2.20: Example of π and σ bonds in nitrogen molecule [23]

The delocalized π-electron cloud over the backbone chain is responsible for the optical and electrochemical properties of CPs, which find application in organic bioelectronics [24].
Among these conducting polymers, PEDOT:PSS is of particular interest due to its properties, including high electrical conductivity, easy doping tunability, high transparency, high mechanical flexibility, excellent thermal stability, and easy solution-processability [25].

2.3.1 PEDOT:PSS

PEDOT:PSS is a polymeric mixed ion-electron conductor with a relatively high ionic conductivity and specific capacitance [26], and it consists of positively charged conjugated PEDOT chains and negatively charged PSS chains, linked through the Coulombic interaction.
PEDOT is a derivative of polythiophene, obtained by the oxidative polymerization of its monomer ethylenedioxythiophene (EDOT) via either an electrochemical or a chemical polymerization. PSS is a polymer surfactant, which not only serves as the counterions for charge-balancing, but also allow the dispersion of PEDOT in the aqueous environment with a ratio of 1:2.5 (PEDOT to PSS) in weight [25].

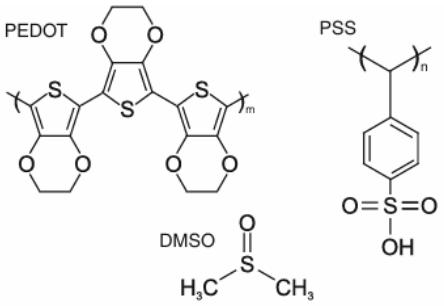

Figure 2.21: Chemical structure of PEDOT, PSS and DMSO [27]

Poly(3,4ethylenedioxythiophene) doped with poly(styrene sulfonate) is the most popular material used as channel in OECTs thanks to its commercial availability and good stability in aqueous environments.
PEDOT:PSS films can be rendered insoluble in aqueous solutions by cross-linking them with (3-glycidyloxypropyl)trimethoxysilane (GOPS), which enhances the adhesion of PEDOT:PSS to the substrate, thereby improving its stability in electrolyte solutions [28].
It has been demonstrated that the thickness of the PEDOT:PSS active layer affects the achieved g_m value, which represents the sensitivity of the device by converting cellular signals to recorded drain-source current changes. Thicker PEDOT:PSS layers typically exhibit higher g_m values, but slower frequency response, which depends on the penetration of the ions into the channel. By decreasing the thickness of the active layer, it is possible to expand the bandwidth, although this may result in a decrease in sensitivity.
This effect can be understood by analyzing the working principle of the device [29]. Applying a positive bias to the gate electrode, the anions accumulate around the gate electrode, while the cations from the electrolyte penetrate into the polymer channel and compensate the pendant sulfonate anions of PSS, leading to a de-doping of PEDOT and as a consequence a decrease in the drain current (p-type behaviour).
In the case of thinner active layer, the de-doping occurs more rapidly, as a smaller quantity of ions is required, resulting in a faster response; however, this also leads to a reduction in drain current and, consequently, in transconductance.
Doping is governed by the following reaction:
$PEDOT^+ : PSS^- + M^+ + e^- \leftrightarrow PEDOT + PSS^- : M^+$, where M^+ are the cations from the electrolyte and e^- are electrons from source electrode [30].

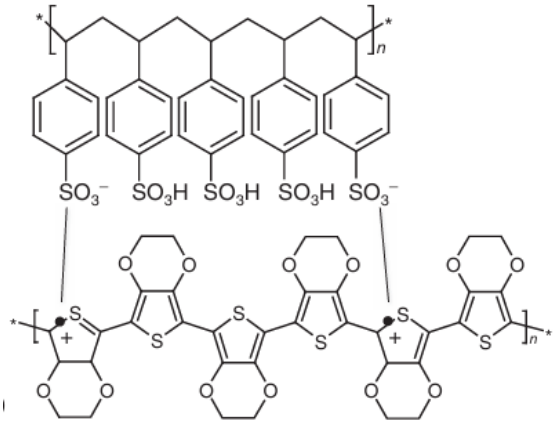

Figure 2.22: Chemical structure of PEDOT:PSS [15]

The use of a secondary dopant, such as ethylene glycol, significantly enhances the conductivity of the polymer, while also enhancing the overall stability of the device [29].
Regarding organic bioelectronics, in order to obtain a very efficient device in terms of sensitivity, functionalization of conducting polymer is the most crucial step. As previously discussed, there are a variety of functionalization techniques that must be employed in order to ensure the stability and preservation of the biological active material.

Chapter 3

Experimental

This chapter outlines the design, optimization and manufacturing processes either for the fluidic platform responsible for sensing and for the microfluidic platform for separating plasma from pure blood.

3.1 Fluidic sensing platform fabrication

OECTs are integrated into the platform responsible for analysis and detection; this platform is based on four main components:

- a holder comprising a top and a bottom part that provides support and alignment for the other parts in a compact package. The bottom and top parts are 3D printed; contacts are fixed on the top part with soldered wires which allow the connection with the measuring system;
- a fluidic sealing made by two polydimethylsiloxane (PDMS) layers bonded together, shown in figure 3.1. The fluidic comprises a straight channel with a width of 1 mm, which is enlarged to 2 mm in correspondence of gate and devices, that connect the two inputs (on the same line) and the output (on the mid-right top area); in correspondence of gates and devices there are three open chambers in the channel;

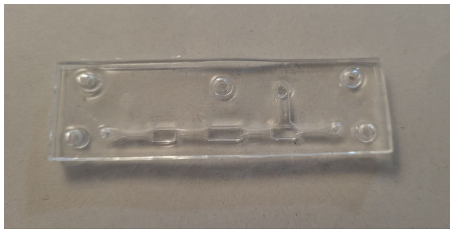

Figure 3.1: PDMS fluidic

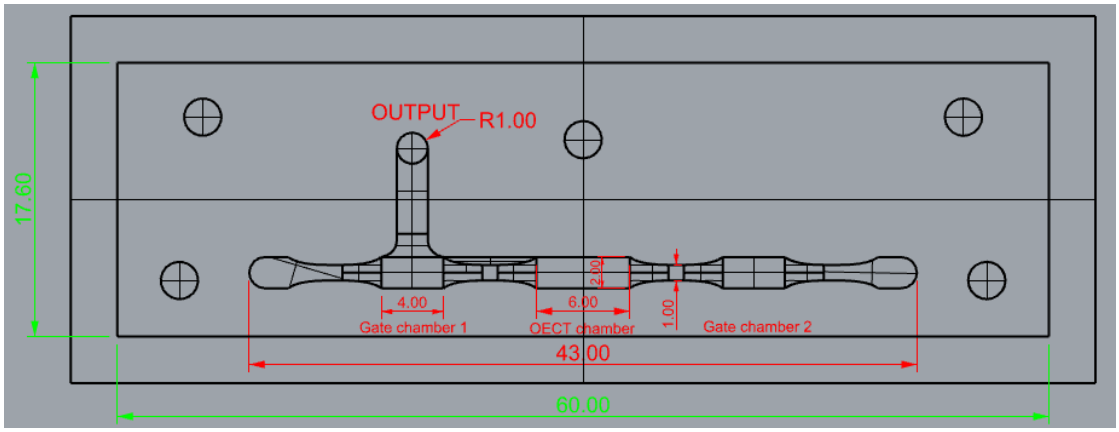

Figure 3.2: Bottom master mold for PDMS fluidic, with dimensions in mm.

- two gold gates patterned on a silicon substrate (Si/SiO_2), that can be functionalized to act as sensing and reference gates; the top gold region corresponds to the area (8 mm^2) which will be in contact with the electrolyte, while the bottom gold region is the area that interacts with the contacts for the measurements;

Figure 3.3: Gold Gate

- the chip containing the three devices (OECTs) with PEDOT:PSS as channel sensing material; the width and the length of the channel are 300 μm and 10 μm, respectively.

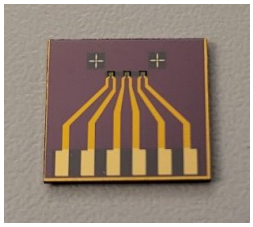

Figure 3.4: Chip with PEDOT:PSS

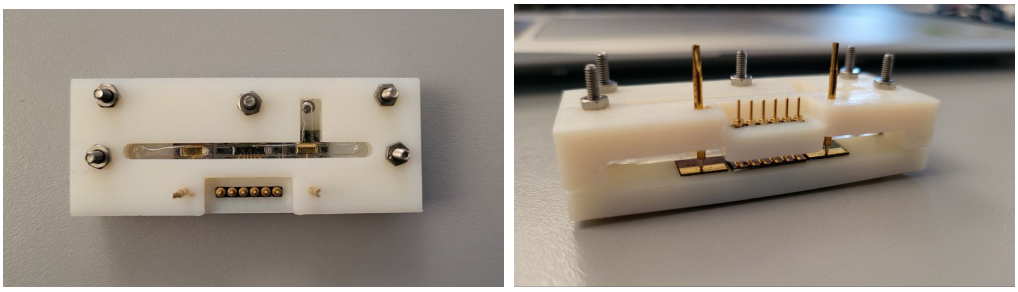

Figure 3.5: Assembled platform top and front view

3.1.1 Objet 3D printer

The bottom and top holders provide support and protection for the fluidic, packaging all the components with precise alignment. The two parts, shown in figure 3.6, are designed using a CAD tool, optimizing the shape in order to solve possible design problems, such as the excessive loading of the contacts on the chip and on the gates. For these reasons, different optimizations are performed:

- the bottom and top parts of the holder are thickened;
- four spacers of different thicknesses on the top holder have been added to provide the right pressure to the PDMS layer (to prevent fluid leakage), limiting the human applicable pressure when the structure is assembled to avoid damages (especially of contacts and/or chip);
- contacts for gates and contacts for source and drain are fixed at different heights in the top holder, due to their different lengths.

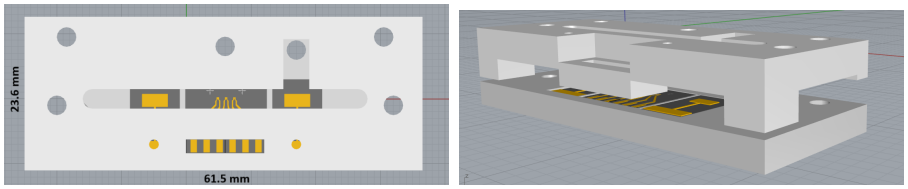

Figure 3.6: CAD top (61.5*23.6 mm) and perspective view

After the design, the holder is printed with Stratasys 3D Objet30 (shown in figure 3.7), a 3D printer that uses a VeroWhite resin and a Sup705 resin for supporting the printing process.
At the end of the printing process, the items are removed from the "tray" and the support material on the bottom of each item (deposited by the printer to facilitate easy detachment) is scraped off; the items are then washed with water and dried.

Figure 3.7: Objet30 3D printer [31]

3.1.2 PDMS

PDMS background

Polymers candidate in biomedical and BioMEMS applications include polycarbonate (PC), polymethylmethacrylate (PMMA), polyvinylchloride (PVC), polyethylene (PE), and polydimethylsiloxane (PDMS) [32].
Of these, PDMS is one of the most exploited, due to its interesting properties, including:

- biocompatibility,
- chemically inert,
- gas permeability,
- excellent resistance to biodegradation,
- thermal stability,
- easy sealing to other surfaces,
- flexibility and stretchability,
- optically transparent,
- low cost.

Due to these properties, PDMS is employed in a variety of biomedical applications, including micropumps, catheter surfaces, microvalves, in vitro studies of diseases, implants, microfluidics, etc. [33]. Due to its thermal and electrical insulation properties, PDMS is employed in the encapsulation of electronic and bioelectronic components, preventing mechanical or environmental damage. Additionally, PDMS

exhibits hyperelasticity, which is the ability of a material to undergo large deformations before rupture; this characteristic is also exhibited by biological tissues, such as blood vessels, which could be mimicked by PDMS. [33].
Despite these advantages, PDMS, due to its CH3 groups, has a hydrophobic surface, which can cause limitations in biological applications, such as microchannels. To overcome the hydrophobicity it is possible to introduce plasma treatment with oxygen, argon, or air [33]. For instance, oxygen plasma can destroy methyl groups ($Si - CH_3$) introducing silanol groups ($Si - OH$), which transform the PDMS surface from hydrophobic to hydrophilic [34]. Subsequently, the activated PDMS surface can be irreversibly bonded to glass, silicon or another PDMS surface within a few minutes. In fact, this process is "self-limited", since oxidized surfaces return to a hydrophobic state, mainly due to the reorientation of silanol groups towards the bulk (hydrophobic recovery) [35].
PDMS has found extensive application in soft-lithography, due to its lower cost compared to photolithography. Furthermore, when a mould is fabricated, it can be reused, which further reduces the overall cost [33].
Soft-lithography comprises [35]:

- replica moulding, in which PDMS structures with micron-scale features, can be fabricated by simply filling a mould and waiting for the polymerization; this process is more cost-effective than using glass or silicon structures and cleanroom environment is not required;

- microcontact printing, based on the flexibility of PDMS and its propensity to adhere to other surfaces;

- rapid prototyping, which translates to less time necessary thanks to CAD programs.

PDMS fluidics

The fluidic channel is obtained by bonding two PDMS layers, which were previously designed by a CAD tool and subsequently obtained by replica moulding technique. The procedure for obtaining the fluidics is:

1. First of all, two master molds, shown in figure 3.8, are printed with the Objet30. The bottom mold comprises a channel (with three "chambers") and an output pillar, while the top mold has only the two pillars for the inlet holes.
   Both molds also have five pillars in order to create the holes for the support screws.

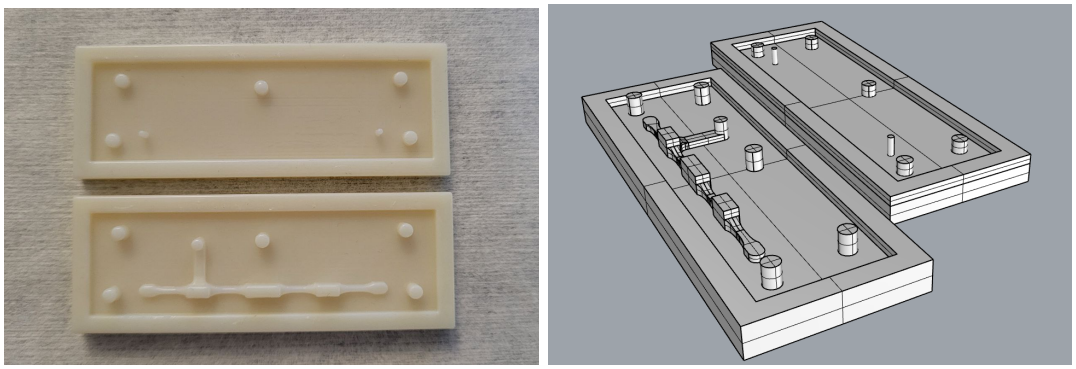

Figure 3.8: Mold for PDMS fluidics, with CAD perspective view on the right.

2. The master molds after the water wash are placed in the oven at 110°C for an "overnight" post-curing process.
   This is an essential step to allow for the PDMS polymerization; in fact, the majority of the stereolithography (SLA) resins contain photo-initiators that can inhibit PDMS curing, leading to sticky PDMS or replication defects.
   For this reason, this thermal treatment is performed before the first PDMS replication in order to deactivate the unreacted components of the 3D printer resins [36], which can cause replication failure.
   Molds are then washed in acetone using an ultrasonic bath for five minutes (at a frequency of 59 kHz), and finally dried.

3. PDMS is obtained from Sylgard 184 Silicone elastomer kit and relies on the mixing of a base and a curing agent with a 10:1 mass ratio. A higher ratio of curing agent results in a faster hardening time, but a more fragile PDMS sample, and vice versa with lower curing agent ratio [33].

4. Air bubbles are formed during the mixing process and could potentially cause issues during the replica step in the mold, so they are removed by placing the PDMS mix in a vacuum chamber for a few minutes.

5. Degassed PDMS is poured into the master molds, with a degassing step performed when the mold is half-full and completely full to ensure uniformity and absence of air bubbles trapped between the mold and the poured PDMS.

6. Molds are then placed in the oven for one hour at 90°C. The curing time depends on the temperature of the oven (higher temperature means less time and vice versa) and on the size of the PDMS sample.

7. After baking, PDMS layers are extracted from the molds using small palette knife, with isopropanol added to facilitate the detachment.

8. The top and bottom layers are finally bonded by depositing a small amount of liquid PDMS in the bottom layer without clogging the channel and placing the top part to seal the channel; the bonded layer is then placed on the hot plate for a few minutes to allow uncured PDMS to act as glue for bottom and top part.

3.2 Biosensor fabrication

The fabrication of OECT and gold gate is conducted in a cleanroom starting from a 4-inch silicon wafer. Wafer is coated with a layer of SiO_2 to grant electrical insulation. The layout is designed using Clewin, starting from a single device and then replicating it to cover the entire wafer area, as shown in the following figures.

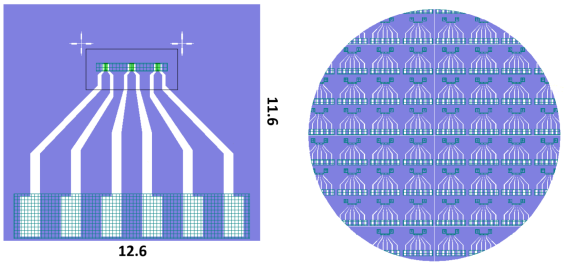

Figure 3.9: Clewin: single OECT and wafer layouts (dimensions in mm).

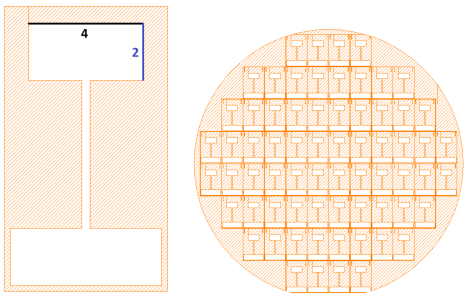

Figure 3.10: Clewin: single gate and wafer layouts (dimensions in mm).

The first step involves the deposition of a gold layer on the entire wafer; prior to this, a layer of titanium is deposited acting as adhesion layer. This initial stage of the fabrication process involves the loading of the wafer into an evaporation system (figure 3.11).

Figure 3.11: Evaporator ULVAC EBX-14D

This is followed by a photolitographic step (illustrated in figure 3.12), which is used to pattern the source and drain electrodes in the case of OECT, or directly the gate in the other case. This is accomplished by using AZ 1518 photoresist in accordance with the following recipe:

1. spinning of the photoresist for 5 seconds at 500 rpm, followed by 30 seconds at 4000 rpm;
2. soft bake at 110°C for one minute;
3. exposure with mask for 6.25 seconds at 8 mW/cm^2;
4. development with AZ 400K developer and water (1:3) for few seconds followed by water rinsing.

This step is followed by a wet etching of the gold and titanium layers. Being AZ 1518 a positive photoresist, the etching removes gold and titanium in correspondence of the region previously exposed, where the photoresist has been removed. Gold is etched using Technietch ACl2, while titanium is etched using titanium etch (with a $HF : H_2O_2 : H_2O$ 1:1:20 ratio).
The fabrication of the gold gate wafer is complete, while for the OECT wafer another photolithographic step is required; in fact, the deposition of a passivation layer is necessary to prevent short-circuit, and with lithography it is possible to open "windows" in the passivation to connect the pads.
In this case AZ 5214 photoresist is employed, as it is optimal for lift-off and, being a negative photoresist (image reversal), the exposed area remains covered by photoresist.

The recipe is the following:

1. spinning of the photoresist for 5 seconds at 500 rpm, followed by 30 seconds at 4000 rpm;
2. soft bake at 105°C for 2 minutes;
3. exposure with mask for 6.25 seconds at 8 mW/cm^2;
4. reversal bake at 105°C for 2 minutes;
5. flood exposure (without mask) for 25 seconds at 8 mW/cm^2;
6. development with AZ MiF 726 developer for 20-30 seconds followed by water rinsing.

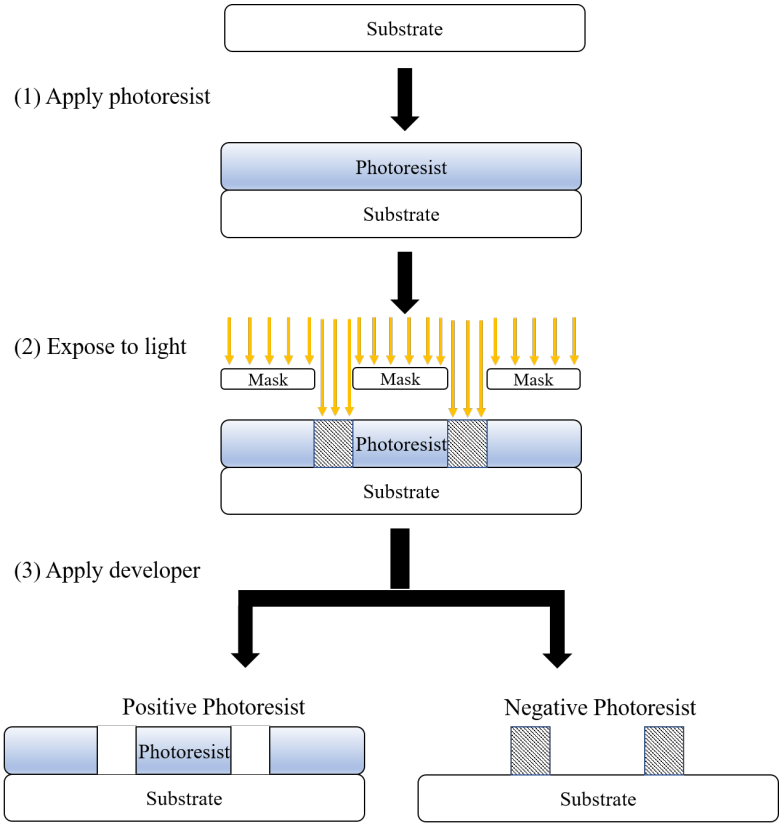

Figure 3.12: Lithographic process [37]

Subsequently, Al_2O_3 (aluminum oxide), which is responsible for passivation, is evaporated on the wafer.

Finally, a lift-off in DMSO is performed for some hours in order to remove the photoresist (and the aluminium oxide on top of it), thereby opening the pads windows.
The final step is the laser dicing of the wafer into individual devices, but before doing this a photoresist layer is spun on the wafer in order to protect it from contamination. The photoresist is removed by washing it in acetone and isopropanol.
During the fabrication process, two interchangeable equipment can be used for the exposure step: a laser writer and a mask aligner, shown respectively in figures 3.14 and 3.13 (left). The former is a direct writing system with a very high resolution, while the latter requires a previously fabricated mask, but it is faster. The choice may be dictated by the convenience of fabricating a mask (an example is shown in the right image of figure 3.13); in fact, if the exposure geometry is maintained unchanged for many wafers, the mask cost could be justified and amortized along multiple exposures.
In our case, a mask is employed for the passivation step, whereas the gate fabrication and the definition of source and drain electrodes are achieved through laser writing, given that these geometries can be modified.

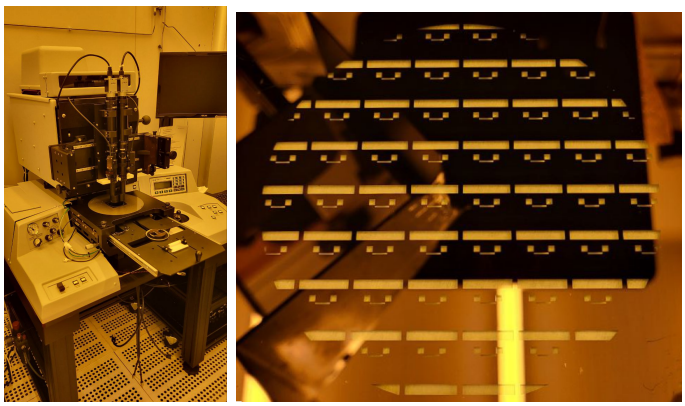

Figure 3.13: Mask Aligner and mask for passivation

Figure 3.14: MICROTECH laser writer LW405 A

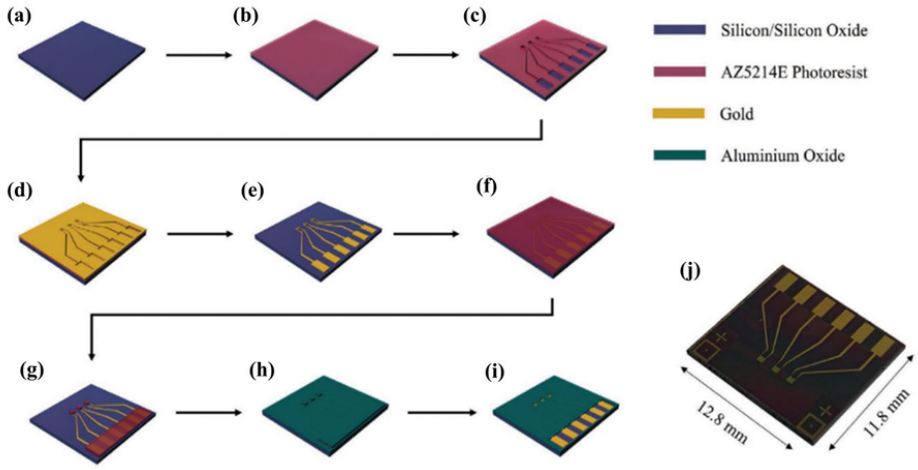

Figure 3.15: Example of fabrication steps for OECT [17]

3.3 PEDOT:PSS deposition

The final step in the fabrication of OECT is the deposition of the organic semiconductor. There are a variety of deposition techniques that can be employed for organic semiconductors, including spin coating (shown in figure 3.16), aerosol printing and inkjet printing.
However, spin-coating for this application is not commonly used since it requires a significant amount of PEDOT:PSS, which is deposited by centrifugal force across the entire chip surface (and subsequently removed to obtain the desired pattern). The aforementioned deposition method results in an uneven distribution, cracks, and coffee-ring effect after baking (the latter is shown in figure 3.24).

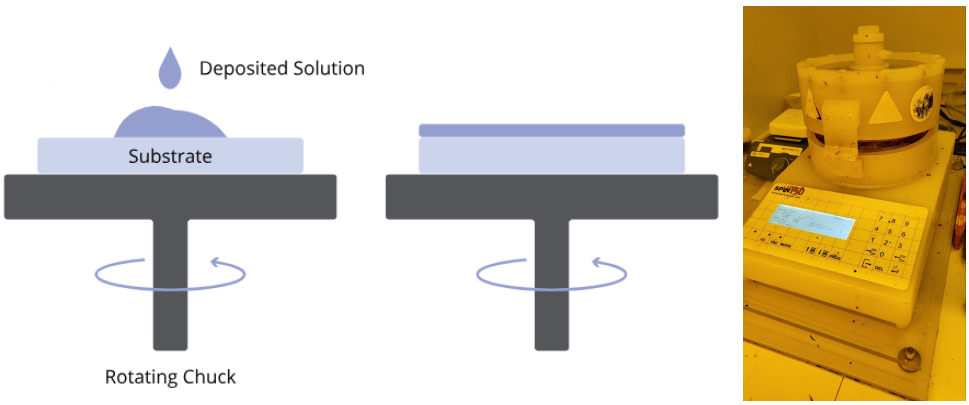

Figure 3.16: Spin Coater and its operation [38]

Consequently, it was decided to employ inkjet printing and aerosol jet printing (the latter for comparative purposes) as deposition technique.
Inkjet and aerosol jet printing processes can be divided into four steps [39]:

1. ink formulation, where stability and jettability are two crucial parameters. Stability is the ability of the ink to maintain its characteristics over time, which requires a narrow particle size distribution and resistance to aggregation, while jettability is the ability of the ink to become expelled droplets.

2. drop deposition, which occurs at a rate of thousands per second;

3. wet film formation, which depends on the distribution of particles; in fact, an inhomogeneous distribution can be observed if ink dries through evaporation (coffee ring effect). Other distribution problems include the satellite formation (for inkjet) and the offset from the desired location, which leads to worse deposition.

4. consolidation, consisting in the removal of solvents after printing.

It has been observed that a plasma treatment of the substrate surface can enhance the ink adhesion [40]. Another method to improve ink adhesion is the deposition of a GOPS adhesion layer (prior to PEDOT:PSS deposition) on the substrate through spin coating. The preparation of this adhesion solution is based on the following formula: 22 mM of GOPS in 200 : 1 of toluene : acetic acid.
A small quantity of solution (around 30-40 μl) is deposited through a micro-pipette onto the chip, followed by a spin coating step (5 seconds at 500 rpm, followed by 60 seconds at 4000 rpm) and a 30-seconds hotplate bake at 120°C.

3.3.1 Inkjet

Theoretical operation

Inkjet printing is a non-contact additive printing technique that involves the deposition of ink microdroplets ejected through a nozzle actuated by a piezoelectric, thermal, or electrohydrodynamic effect. Inkjet is very suitable for both production and research purposes, since it is a digital technique and so print pattern can be changed fast and with low-cost impact, compared to other manufacturing techniques. Furthermore, it is biocompatible and friendly to the environment. Another advantage is that inkjet requires very little material, which leads to the formation of layers less than 1 μm (100–500 nm), and the printing of only the designed pattern [41].
The printing process, reported in the figure 3.17, essentially involves the ejection of a fixed quantity of ink, through a nozzle, from a chamber filled with liquid which

contracts in response to an external voltage (piezoelectric effect). This sudden reduction creates a droplet that falls, by gravity, until it impinges on the substrate and then it dries through solvent evaporation. These falling droplets are affected by a number of factors, including jetting conditions and environmental properties; for instance, a more viscous ink creates a liquid column and small droplets, while higher voltages result in separated droplets.

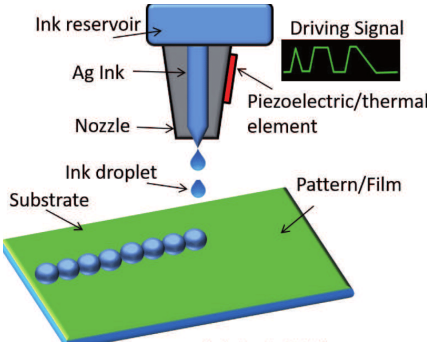

Figure 3.17: Inkjet operation [42]

Recent studies have shown that droplet spreading and the final printed shape are strongly dependent on viscosity, which is a function of the molar mass of the polymer [43].
The phenomena responsible for the droplet formation can be characterized by dimensionless numbers such as Reynolds number, Weber number and Bond number:

$$\mathrm{Re} = \frac{\text{Inertial force}}{\text{Viscous force}} = \frac{\rho v D}{\eta}, \mathrm{We} = \frac{\text{Inertial force}}{\text{Surface tension}} = \frac{\rho v^2 D}{\gamma}, \mathrm{Bo} = \frac{\rho g D^2}{\gamma}$$

where ρ is the fluid density, η is the shear viscosity, γ is the surface tension, D is the droplet diameter, and v is the droplet velocity.
Bond number refers to the effect of gravity, but can be neglected for micron-sized droplets, while the ratio between Re and $\sqrt{\mathrm{We}}$, defined as Z number, relates the viscous forces to surface tension forces and it is used to predict the jetting behavior of droplets:

$$Z = \frac{Re}{\sqrt{We}} = \frac{\sqrt{\rho \gamma D}}{\eta}$$

A rule of thumb for the formation of optimal droplets is that $1 < \mathrm{Z} < 14$ [44].
As regards the ink, one of the most common conducting materials employed is PEDOT:PSS, while regarding the substrates, inkjet printing is utilized on flexible substrates such as PET and Kapton, or on rigid substrates such as glass and silicon [41].

Software & setup

The inkjet installed at in *Chilab* is a Jetlab 4 from MicroFab Technologies, shown in figure 3.18. It has a single interchangeable piezoelectric nozzle with a diameter of either 50 or 80 μm, depending on the desired diameter size.
The printing platform is capable of moving mechanically in both the x and y direction, allowing the substrate to be positioned under the nozzle, which instead can be moved in z direction to focus and print at different heights.
Two cameras are present, a lateral one to observe the formation of the droplets, and one on top that is used to align the nozzle to the "origin" of the substrate, in general by using markers.

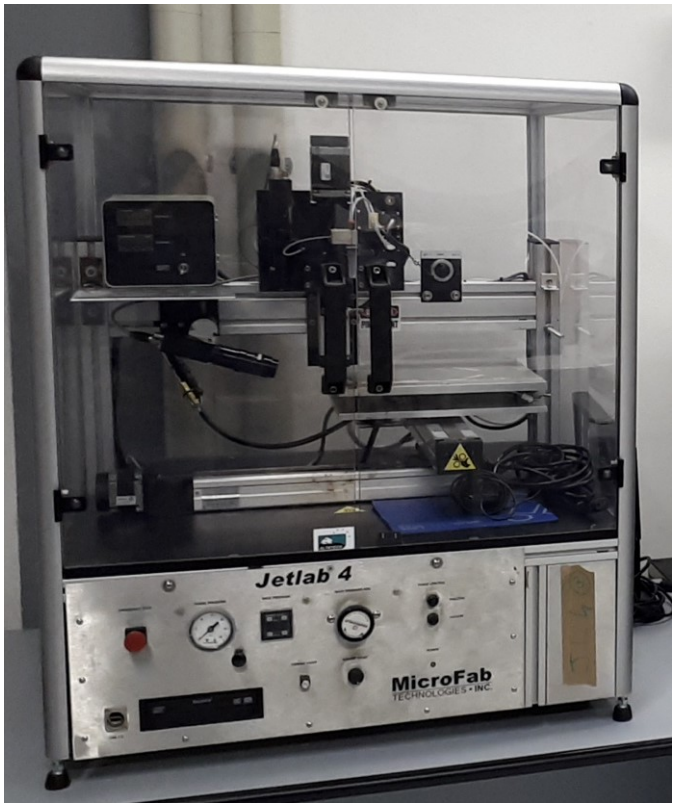

Figure 3.18: Jetlab 4 Inkjet printer

Additionally, the software *jetlab4.exe* enables the user to adjust the printing parameters and initiate the printing of a pre-imported pattern, which is obtained from *gds2jetlab.exe* that converts the pattern file created by the user on CleWin, as visible in figure 3.19.
Upon importing the pattern, it is necessary to set the origin and the x direction for the printing process and additionally, it is possible to adjust 3 parameters:

- spot spacing, which corresponds to centre-to-centre distance between two droplets impacting on the thickness, and in general the lower, the more overlap between droplets, and thus the higher the thickness of the obtained layer; this depends also on the droplet size, since if the droplet is very small it is necessary to decrease the spacing in order to fill the entire print pattern without leaving uncovered space between droplets;
- spot margin, which corresponds to the distance between the centre of the droplet and the margin of the print pattern that in general is maintained as lowest as possible;
- fly velocity, which corresponds to the velocity of the nozzle during the printing, related also to the frequency of ejection.

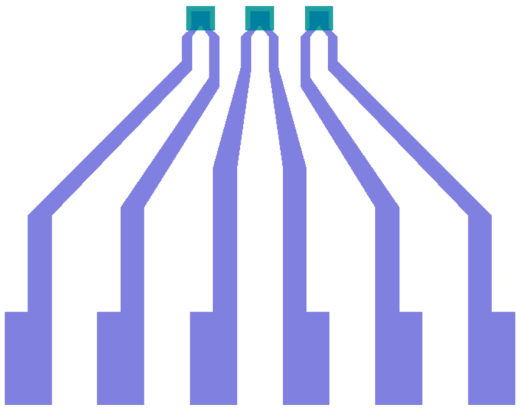

Figure 3.19: Example of file from Clewin, with the print pattern in green

By setting the parameters, the optimal waveform can be obtained to print small droplets and remove satellites. Waveform may be unipolar or bipolar, but the latter is recommended to ensure the removal of the residual droplets. In fact, an increase in voltage corresponds to an expansion of the fluid, while a decrease in voltage corresponds to a fluid compression.
Adjustable parameters, which can also be observed in the figure 3.20, are:

- rise time, corresponds to the 'push action' during which the fluid expands as result of piezoelectric actuator contraction;
- fall time, corresponds to the 'pull action' during which the fluid contracts as result of piezoelectric actuator expansion;
- dwell time, is the time between push and pull and corresponds to the pulse amplitude;

- echo time, determines the combination of the pressures induced at t_{fall} and $t_{finalrise}$ to reduce the pressure shock in the negative pressure period and adjust the droplet shape removing any residuals [45] (residuals present in figure 3.21);
- dwell voltage, positive voltage that causes the expansion of the piezoelectric actuator; an increase of this value results in a proportional increase of the droplet volume;
- echo voltage, negative voltage which cause the contraction of the piezoelectric actuator; in optimal case it has the same (absolute) value of the dwell voltage.

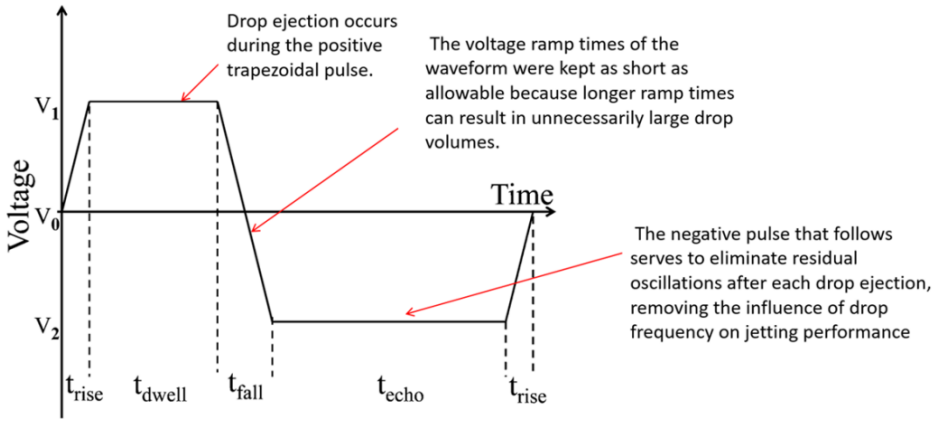

Figure 3.20: Example of bipolar waveform [46]

Figure 3.21: Droplet with satellite

Another crucial factor influencing droplet formation is back-pressure, expressed in ψ, pound per square inch, which corresponds to 0.06805 atm. It can be manually adjusted by rotating the handle in the front panel and observing the actual value in the display on the left.
Initially, a positive pressure is applied to push the ink from the reservoir towards the nozzle, then the pressure is set to negative in order to obtain the formation of droplets.
Typical values of back-pressure to obtain droplets with optimal volume and shape, in the case of PEDOT:PSS ink, are demonstrated to be in the range of -8 ψ to -12 ψ. Values greater than -8 ψ result in the ink being directly ejected without the formation of droplets of correct shape and volume, while values below -12 ψ result in the ink returning back in the reservoir.
Considering all the other parameters, with the exception of the previously defined back-pressure, the optimal results, which correspond to the droplet of the figure 3.22, for PEDOT:PSS printing are achieved with the following values:

PEDOT:PSS print parameters	
Parameter	Value
Rise time 1	3 μs
Dwell time	12-40 μs
Fall time	6 μs
Echo time	12-40 μs
Rise time 2	3 μs
Idle voltage	0 V
Dwell voltage	30 - 45 V
Echo voltage	30 - 45 V
Frequency	1000 Hz
Spot margin	1 μm
Spot spacing	50 or 80 μm
Fly velocity	25 mm/s

Figure 3.22: Ejection of a well-defined droplet

A small deviation from these parameters could be observed if the nozzle is changed with one of different diameter.
Following the printing phase, the printed chip is left to dry at ambient temperature for approximately 20-30 minutes; subsequently, the chip is placed in an oven at a temperature of 150°C for 30 minutes; this latter step constitutes annealing treatment, which is performed with the objective of removing the solvent and the excess of water present in the ink, thereby causing a shrinkage of the film thickness. Annealing increases the performance and the conductivity of the device if it is performed in a range between 120°C and 250°C; however, if the annealing temperature exceeds this range, the device's performance is dramatically reduced

due to the damaging of the film surface [47].

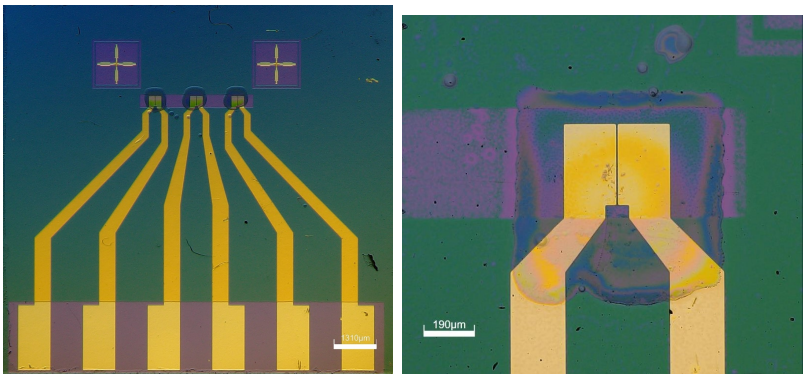

Figure 3.23: Chips printed by Inkjet

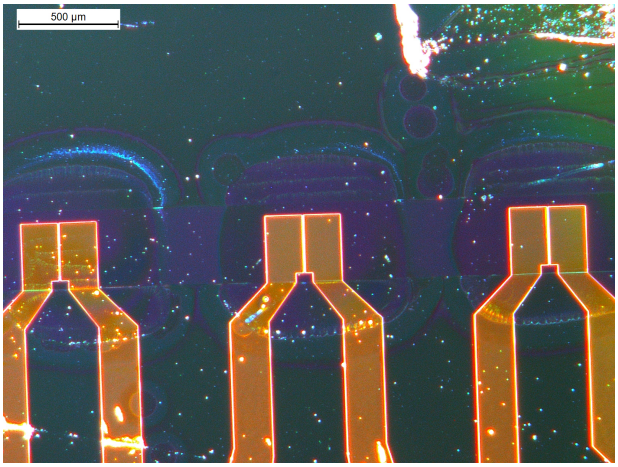

Figure 3.24: Example of coffee-ring effect after the baking

One of the main problems in inkjet printing is the nozzle clogging due to the presence of 'large' particles dispersed in the ink. When these residuals reach the orifice of the nozzle, they can clog, entirely or partially, the ink flow, leading to:

- the formation of droplets with undesired volume/size,
- non-perpendicular flow towards the substrate,
- no-printing due to complete nozzle clogging.

When a clogging event occurs, it is necessary to remove the nozzle from the inkjet and clean it using syringes and distilled water, by following the steps below:

1. connect the nozzle, through an adapter, to a syringe;

2. put the nozzle inside a falcon with distilled water, previously filtered with a 0.22 μm filter to remove additional particles;

3. suck with the syringe in order to fill it with filtered water transporting also residuals that were in the nozzle;

4. disconnect the nozzle and empty the syringe in a waste container;

5. fill another syringe with filtered water and connect it to the nozzle, through the adapter;

6. empty the syringe in a waste container by pushing the filtered water through the nozzle;

7. repeat the entire process until the nozzle seems clean and the flow is straight.

It has been observed that the frequency of clogging events can be reduced by filtering the ink with a 0.22 μm filter and subsequently diluting it 1:1 in water, without affecting the performance.

3.3.2 Aerosol jet

Theoretical operation

As inkjet, aerosol jet printing is a digitally controlled technique for the deposition of droplets in patterned locations (represented in figure 3.25).
Here the ink is stored in a reservoir and "atomized" by a pneumatic or ultrasonic mechanism; then aerosol mist moves towards the print-head carried by a sheath gas, which collimates the aerosol beam and focuses it, thereby improving the precision and resolution, which can reach 10 μm [39]. The focusing ratio, defined as the ratio of the sheath gas flow rate to the carrier gas flow rate, is a key parameter for the printing of fine features, as it minimizes the overspray [40]. The ultrasonic atomizer produces highly uniform aerosols, but only inks with low viscosity can be used, while the pneumatic atomizer overcomes the viscosity problem, but at the cost of uniformity [40].
Material impinging on the walls is not printed, resulting in a change in the deposition rate due to losses, which can be divided into gravitational settling and diffusion.
After the ejection, aerosol droplets impact on the substrate and the focusing efficiency, which describes the broadening of the impact pattern, is affected by nozzle orifice, flow rates and droplet size [48].

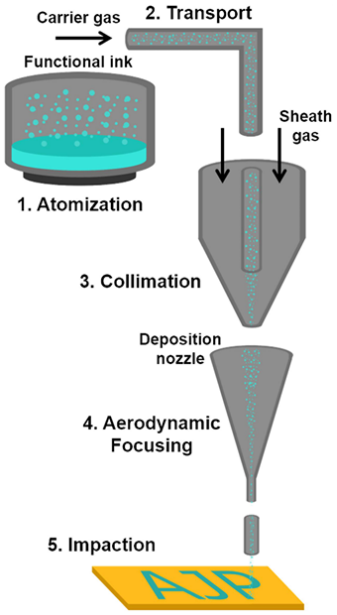

Figure 3.25: Aerosol jet operation [48]

As regard the particle size, there are three requirements [39]:

- particle does not clog the nozzle;
- size distribution must be controlled, otherwise it could change during printing;
- solvent vapor pressure must be tuned, so that the fluid does not evaporate before reaching the substrate

In AJP, achieving reproducibility could be challenging to achieve, and the printing parameters may need to be adjusted when using different materials; however, compared with conventional inkjet, it demonstrates an improved resolution [49].

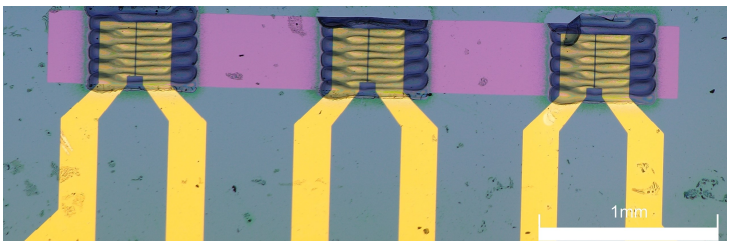

Figure 3.26: Chip printed by aerosol jet

3.3.3 Profilometer

In order to facilitate a direct and precise comparison of the performance obtained from the different deposition techniques, it is necessary to evaluate the thickness of the printed layer. This can be achieved by measuring the step height with a stylus profilometer, shown in the left image of figure 3.27; its working principle, represented on the right image of figure 3.27, is based on a tip that physically touches the surface moving along the sample, in the selected direction, thereby providing a measure of a step with high Z resolution. The feedback system acquires the data and transmits it to the post-processing software. It is important to note that this technique may result in damage to certain surfaces.

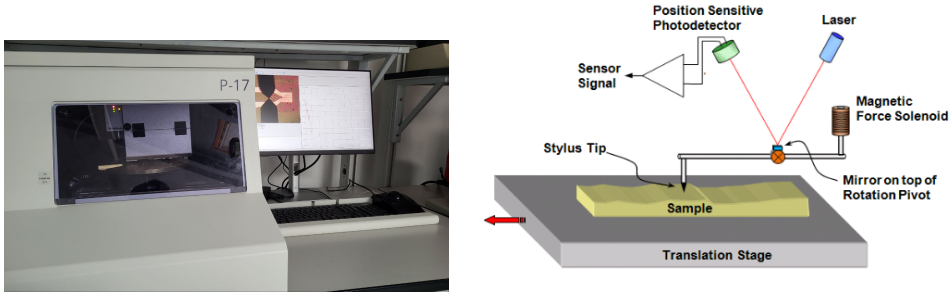

Figure 3.27: KLA TENCOR P17 profilometer and its operation [50]

3.4 Measurement setup

Electrical characterizations are conducted using a Source/Measure Unit (SMU), which in our case is the Keysight B2912A shown in figure 3.28, in conjuction with a probe station.
This unit has two channels, which interface the device through triaxial cables:

- CH 1 is used to apply V_{DS},
- CH 2 is used to apply V_{GS}.

Figure 3.28: SMU [51]

In both cases, the source is connected to ground and by applying voltage it is possible to measure I_{DS} or I_{GS}, depending on how the channels are set, obtaining transcharacteristic and output characteristic plots.
The parameters for the measurement are set through the *QuickIV* software installed on an external computer that is communicating with the SMU through a USB port.
After initiating the communication with the channels, the user can define parameters such as start/stop, compliance, range, trigger and period are defined in order to obtain the desired voltage waveform.
In particular, the compliance current refers to the maximum supportable current, which is set to protect the device, the trigger is used in "timer" mode to scan the period between one voltage point and the next one, and the period (which is a parameter of the trigger) corresponds to the scan rate (the speed at which the applied voltage changes).

For the transcharacteristic, V_{DS} is set at a constant value of -0.2 V, while V_{GS} has a triangular shape between -0.6 V and 0.6 V, with a return to -0.6 V, repeated from three to five times to enhance the stability, as reported in figure 3.29; in general, the most reliable and stable curve is that of the last cycle, or alternatively, an average is extracted, excluding the first cycle.
In the output characteristic, reported in figure 3.30, V_{GS} is varied using a step-function which progresses from -0.2 V to 0.6 V, with a 0.1 V increment. Concurrently, for each step V_{DS} decreases linearly from 0 V to -0.6 V.

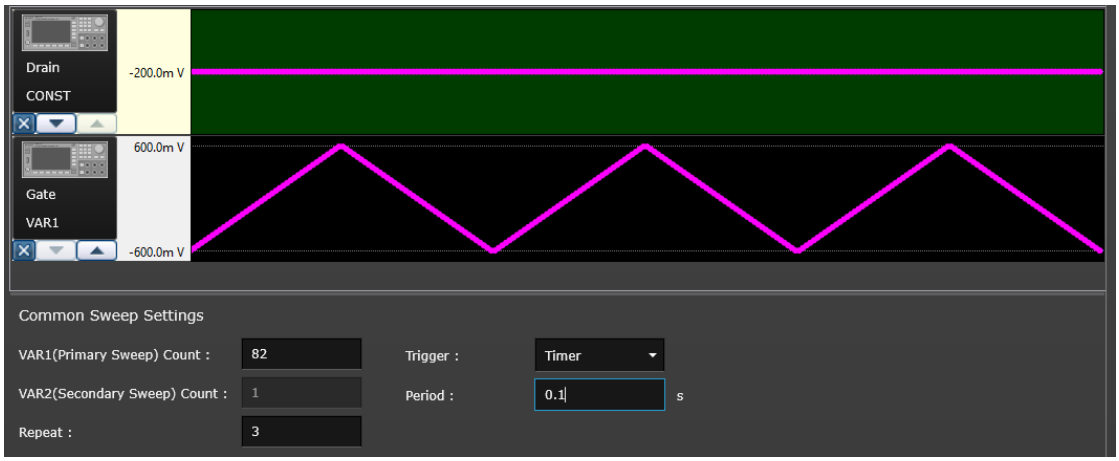

Figure 3.29: Transfer waveform

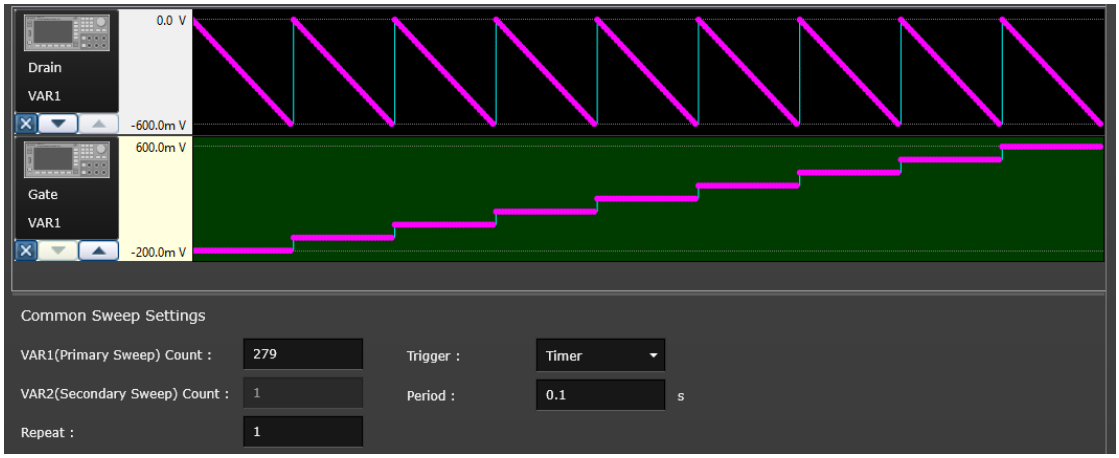

Figure 3.30: Output waveform

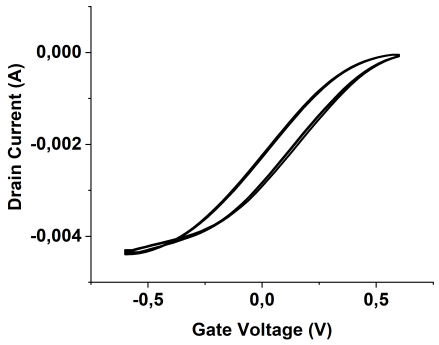

Figure 3.31: Example of transcharacteristic

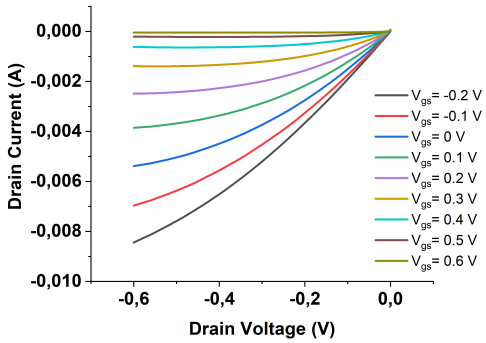

Figure 3.32: Example of output characteristic

In order to verify the correct functioning of the OECT, a fundamental measurement methodology involves bonding a PDMS chamber directly to the chip and subsequently filling the chamber with an electrolyte, such as PBS 0.1 M or NaCl, in which the gate (Au or alternatively Ag/AgCl and Pt) is immersed. In this configuration, a narrower gold gate, shown in figure 3.33, is created, keeping the active area unchanged.

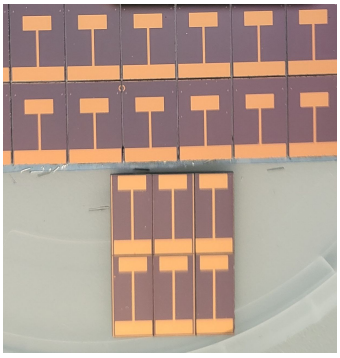

Figure 3.33: Narrow gates (bottom) compared to the ordinary ones (top)

Source and drain are connected to the SMU through micro-manipulators, while the gate is connected through a crocodile cable.
However, this system, visible in figure 3.34, requires long setup time and many PDMS chambers (one for each chip); furthermore, there is a risk of contamination of the device during the PDMS chamber bonding process.

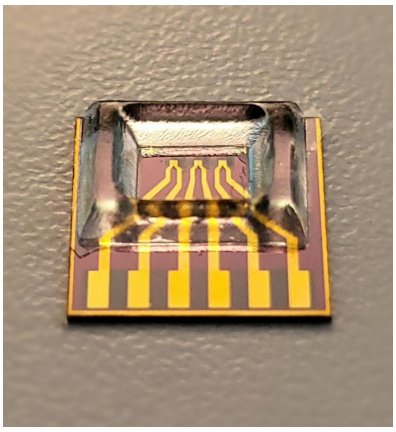

Figure 3.34: Chip with bonded PDMS chamber

For these reasons, a "bridge" mold, shown in figure 3.36, and an appropriate PDMS chamber, show in figure 3.35, are created. PDMS chamber has been designed with the following characteristics:

- total height of 5.5 mm, with an internal step of 0.5 mm at the bottom to avoids the direct contact between the gate and the chip; the total height ensures that the entire gate active area is immersed (the end point is at 4.25 mm from the bottom edge);
- the internal length of the chamber is shorter than that of the gate, but two "slots" 600 μm wide are designed in the chamber (50 μm wider than the thickness of the gate); this allows the gate to be "fixed" in a central region of the chamber without moving.

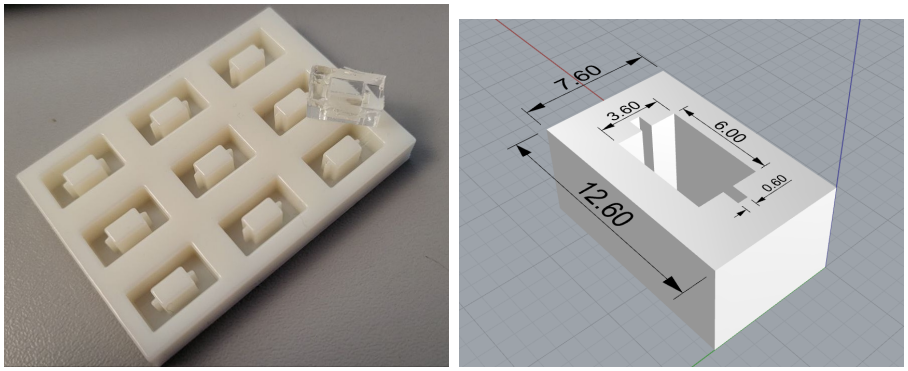

Figure 3.35: Mold and PDMS chamber (with prospective CAD view on the right)

This method obviates the necessity for bonding, thereby reducing the number of required PDMS chambers, since the chamber is pressed by the mold, preventing liquid leakages. Furthermore, the use of micro-manipulators is avoided since the mold has integrated contacts that can be easily connected directly with crocodile cables, as shown in figure 3.37, thus facilitating a rapid switch between the devices.

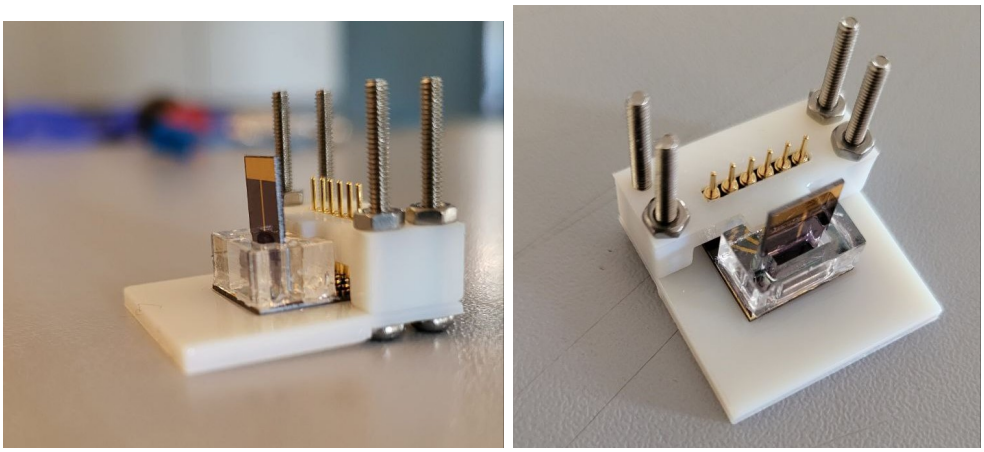

Figure 3.36: Bridge configuration assembled

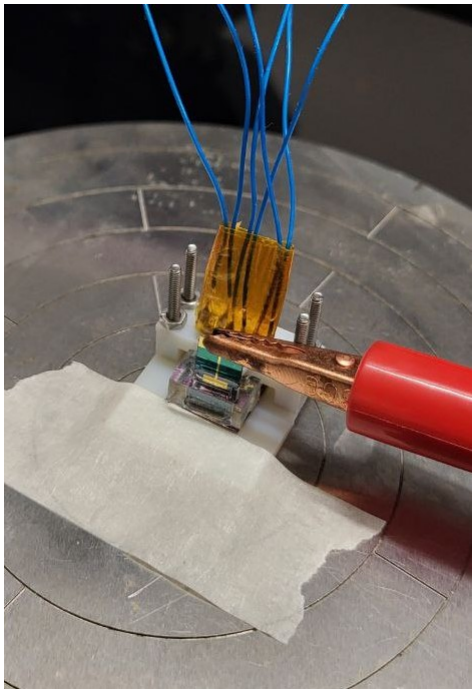

Figure 3.37: Example of measurement test with bridge configuration

Finally, the developed fluidic permits to perform electrical characterization and also biosensing measurements; this structure, visible in figure 3.38, has a planar gate configuration, in contrast to the previously mentioned cases, where the gate is perpendicular to the OECT.

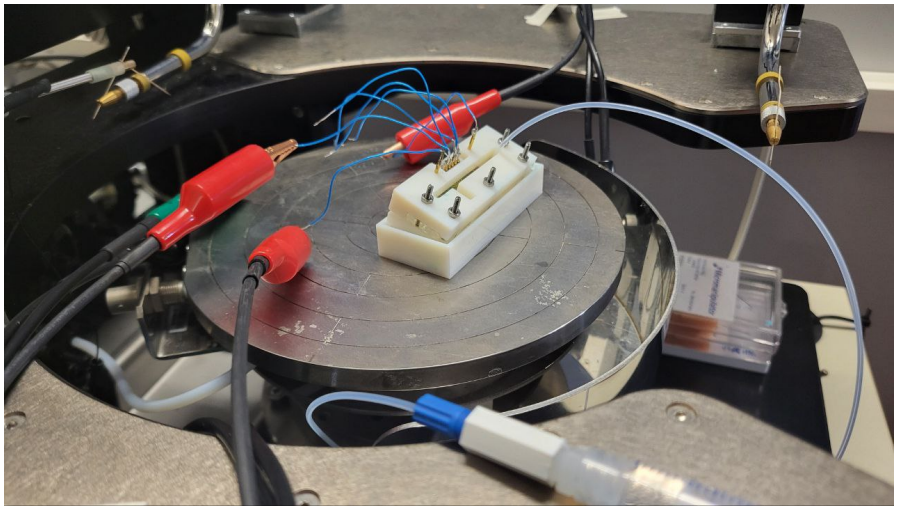

Figure 3.38: Example of measurement test with assembled fluidic sensing platform

3.5 Microfluidic Blood/Plasma separator fabrication

The starting point for the development of microfluidic for blood-plasma separation (BPS) is derived from another project, which consists in a BPS integrated with a blood typing detector to determine the blood group from both direct and indirect methods simultaneously. The proposed design separates blood cells from plasma by applying hydrodynamic forces, overcoming clogging problems and maximizing the volume of the extracted plasma [52]. Our project is interested only in the BPS, which can be divided into two bonded parts:

- PDMS part on top, with branched microfluidic channels responsible to capture red blood cells (RBCs);
- etched glass on bottom, which collects the separated plasma.

Studies report that the optimal configuration for the side channel is the "misaligned-lopsided" configuration [52], as illustrated in figure 3.39.

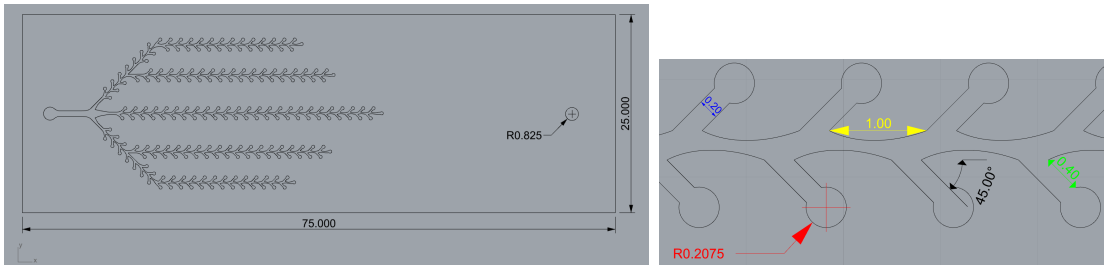

Figure 3.39: Microfluidic CAD of PDMS layer design, with dimensions (in mm) highlighted on the right

This configuration is capable of directing particles towards the sides of the main channel with greater force, thereby delaying the clogging effect and facilitating the extraction of high volume of plasma with high purity. The fundamental principle underlying this upper part relies on hydrodynamic forces: bubbles are generated in the extensive area of the corrugated channel, but they vanish due to the permeable nature of PDMS, which retains the RBCs to the end of side channels [52]. The upper layer is manufactured through soft lithography, which involves first realizing the mold, visible in figure 3.40, with the desired features (as described in 3.1.2).

Figure 3.40: BPS mold

In particular, there are five channels, 50 μm deep, of equal length branching from the inlet and each of them has side channels of 0.4 μm, since long dead-end branches show a better hydrodynamically capture of RBCs in the dead-end zones. All the other dimensions can be seen in the following images. The channels' region occupies approximately half of the length of the PDMS layer, with an outlet situated on the opposite side.
The bottom part consists of an etched glass with an array of pillars having a diamond shape, which has been shown to have the minimum fluidic resistance compared to other shapes such as circular, elongated, pine and rectangular [52]. This region acts as a "plasma collection chamber" connected to the output, through which extracted plasma is sent in order to interface with the OECT detection environment.
To achieve this, a photolitographic step with AZ 1518 as resist is firstly performed to impress the desired geometry, reported in the figure 3.41, through the mask aligner (shown in figure 3.42), with an exposure time of 40 seconds; the glass slide is then developed in 3:1 H_2O:AZ 400K for 30 seconds. Finally, a 7:1 buffered oxide etch (BOE) is conducted for 90 seconds to etch the glass in a highly controlled manner, resulting in a depth of $\sim$ 1 μm, which is less than the minimum RBC diameter (2 μm) to prevent them from escaping from the channels and achieving 100% plasma purity.

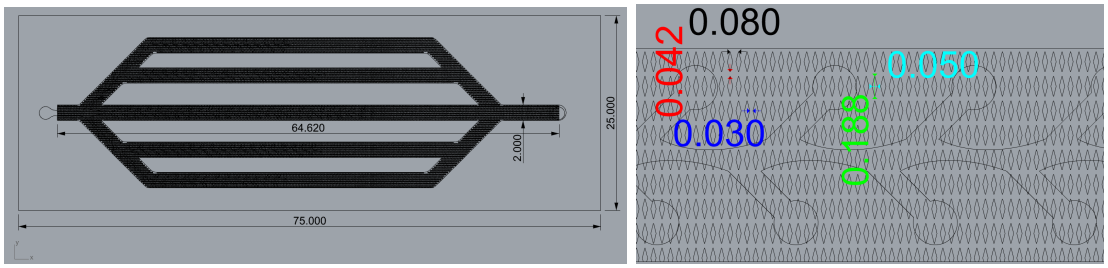

Figure 3.41: Mask CAD for glass etching, with a pillar zoom on the right: Dimensions are expressed in mm.

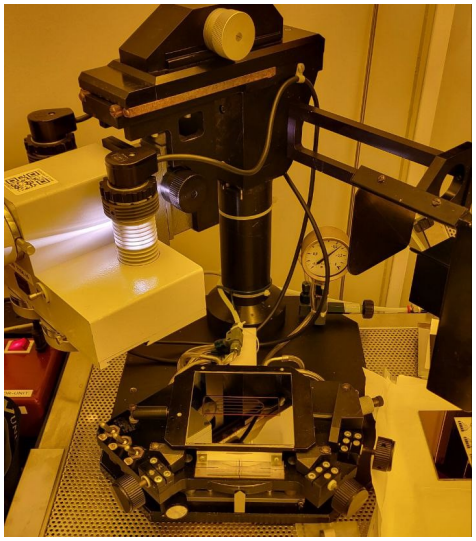

Figure 3.42: Mask aligner setup

Finally, the two parts are bonded through oxygen plasma, which activates the surface of the two layers. Before the treatment, the PDMS layer is washed in ethanol in an ultrasonic bath, leaving "exposed" the surface to bond; then the PDMS layer is placed on a hotplate, again exposing the surface to bond, in order to evaporate the remaining solvent. Subsequently, the plasma treatment can be initiated, with plasma time process set to 30 seconds, as shown in figure 3.43.
Finally, the PDMS and the etched glass are bonded exerting light pressure (at the edges to avoid clogging of the channel) and the final structure (shown in figure 3.44 with dimensions of 75x25x4 mm) is placed on a hotplate at 80°C for 3-4 minutes to improve the bonding.

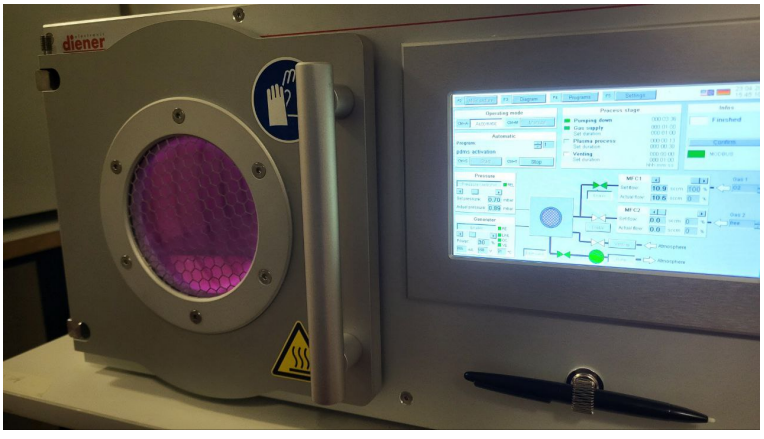

Figure 3.43: Oxygen plasma equipment

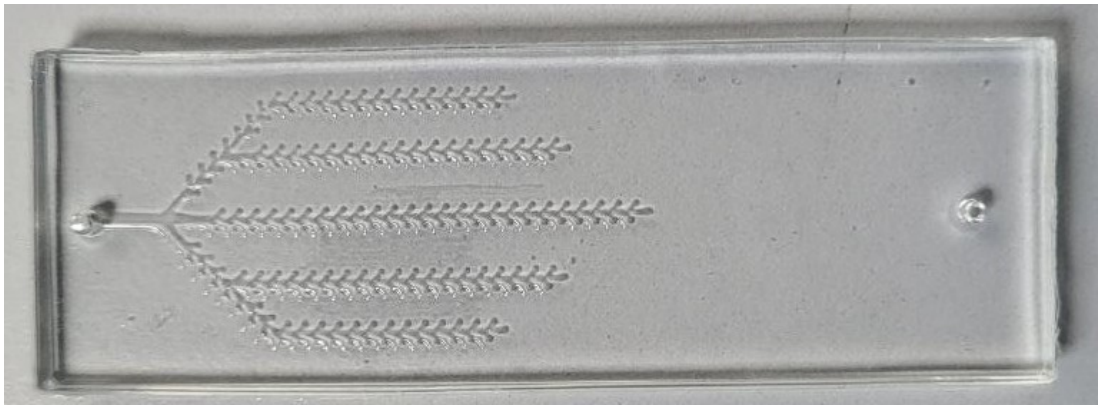

Figure 3.44: Complete BPS

Chapter 4

Results and Discussion

4.1 PEDOT:PSS ink formulation

A variety of PEDOT:PSS inks are available for printing. A commercial solution, Clevios P JET XN, was tested, but with poor results; consequently, the ink was prepared by combining the following substances:

- Clevios PH 1000, which is the organic semiconductor;
- Ethylene glycol, which enhances the conductivity;
- Dodecylbenzenesulfonic acid, which is a surfactant that reduces the surface tension allowing a better relaxation on the substrate;
- (3-glycidyloxypropyl)trimethoxysilane, which is a cross-linker that improves the adhesion and the uniformity of the droplet on the substrate.

Different formulations have been developed, varying the EG concentration in weight (compensated with a variation of Clevios), as reported in the following table.

PEDOT:PSS ink formulation (in weight)				
Substance	Concentration	Concentration	Concentration	Concentration
Clevios PH 1000	93.5%	95.5%	96.5 %	97.5%
EG	5%	3%	2 %	1%
DBSA	0.5%	0.5%	0.5 %	0.5%
GOPS	1%	1%	1 %	1%

4.2 Measurements

As previously stated, the period parameter in measurement software is indicative of the scan rate; in the case under analysis, the period corresponds to the time between two adjacent points of the voltage sweep, thereby indicating that the scan rate is a measure of the speed with which data can be collected.
A shorter period of time corresponds to a faster but "rough" measurement, while a longer period of time corresponds to a slower but "smooth" measurement.
For this reason, measurements are extracted using two periods: 0.1 s and 0.5 s.
Scan rate is obtained by the following formula:

$$\text{scan rate} = \frac{\text{voltage sweep interval/var count}}{\text{period}} \text{ expressed in V/s.}$$

The following table shows the parameters used during the transcharacteristic measurements and the corresponding scan rate.

Transcharacteristic			
Voltage sweep	Var count	Period	Scan rate
-0.6 V ÷ 0.6 V	41	0.1 s	292.68 mV/s
-0.6 V ÷ 0.6 V	41	0.5 s	58.53 mV/s

A preconditioning protocol is established in order to improve the performance and the stability of the devices.
The main points of this protocol are:

- use of fresh GOPS, otherwise the cross-link effect, and the subsequent adhesion of PEDOT:PSS on the substrate, decreases;

- overnight soak the devices in deionized water, in order to remove the remaining low molecular weight compounds from the PEDOT:PSS.

An additional point that could be included in the protocol is a preconditioning cycle of measurements, performed in order to further stabilize the devices [28].
After drying the devices, the microfluidic platform is assembled and filled with PBS 0.1 M waiting few minutes before starting the measurements.
All the prepared ink configurations were subjected to testing to identify the optimal candidate that exhibits superior current modulation and stability, thereby enabling the detection of protein binding on the functionalized gate to be distinguished with greatest clarity.
Measurements are conducted using Ag/AgCl, Pt and Au gates, with a particular emphasis on those obtained with the latter.

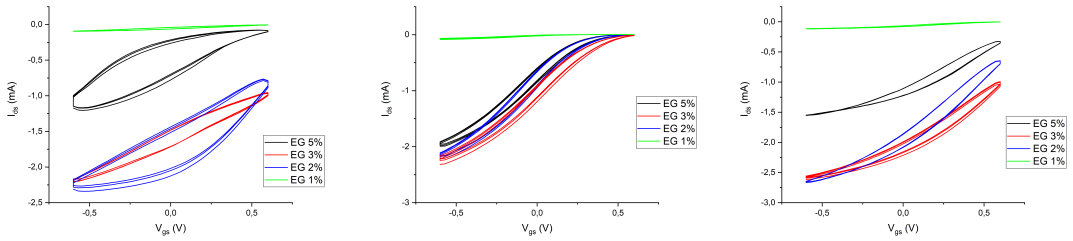

Figure 4.1: Transcharacteristics ink comparison obtained from different gates: Au on the left, Ag/AgCl in the middle, Pt on the right.

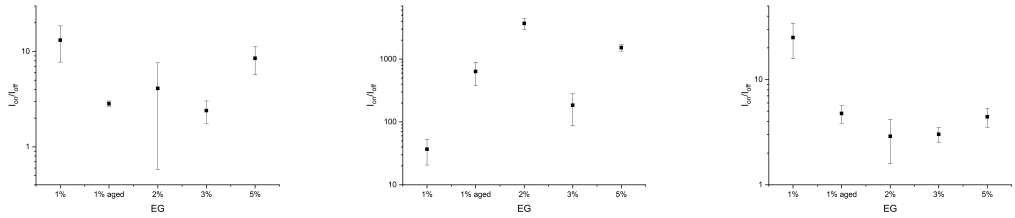

Figure 4.2: I_{on}/I_{off} ink comparison (with y-error bars obtained by calculating the mean value and standard deviation of data from different devices for the same ink) obtained from different gates: Au on the left, Ag/AgCl in the middle, Pt on the right. The term "aged" in the x-axis refers to devices printed with an ink made few days earlier, compared to others printed with an ink made the same day of printing.

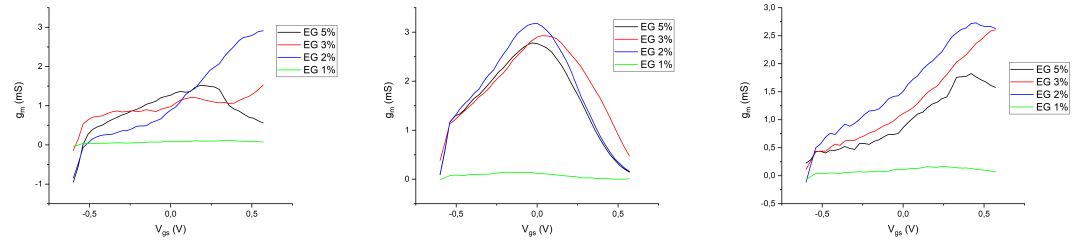

Figure 4.3: Transconductances ink comparison obtained from different gates: Au on the left, Ag/AgCl in the middle, Pt on the right.

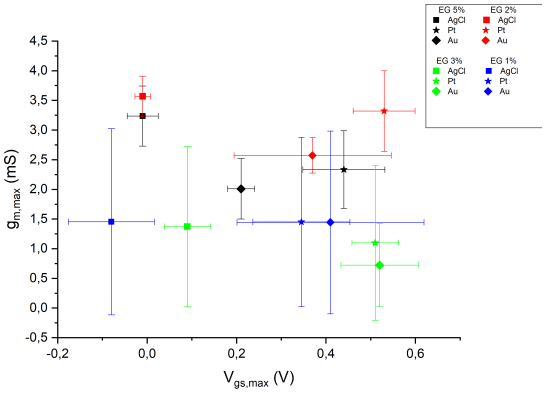

Figure 4.4: Maximum transconductances ink comparison obtained with different gates. The graph illustrates the x-error and y-error bars, which have been obtained by calculating the mean value and standard deviation of transconductance and corresponding V_{GS} for different devices under different ink configurations.

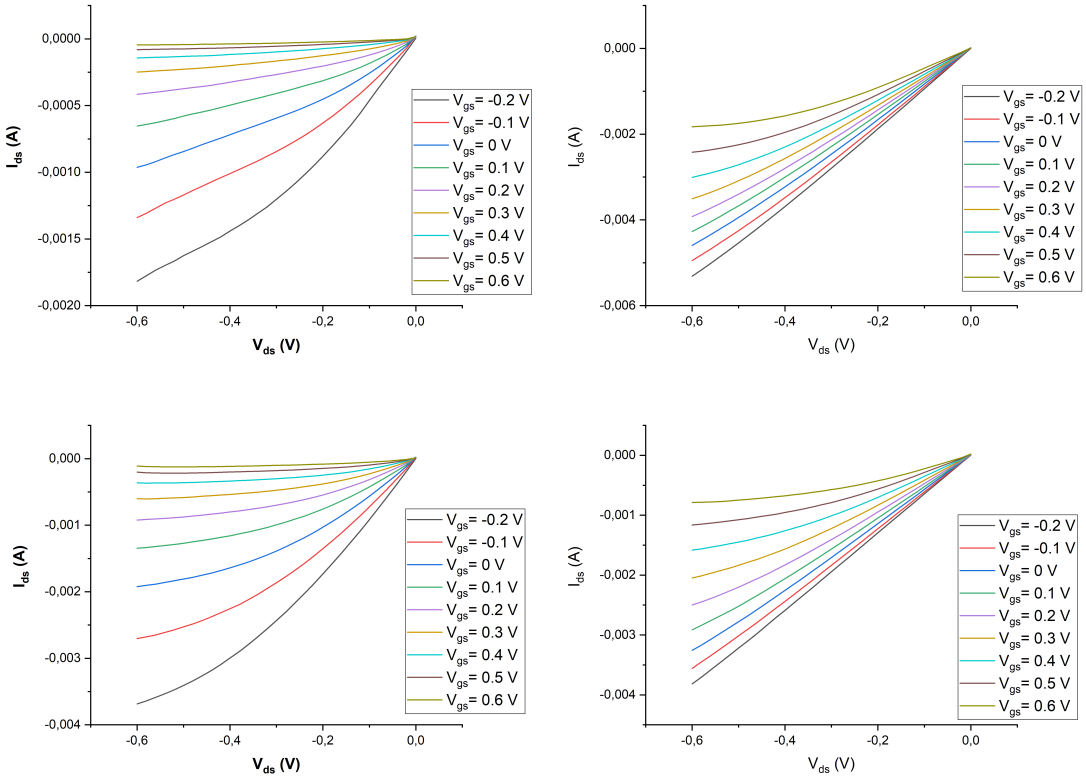

Figure 4.5: Different output characteristics obtained with Au gate.

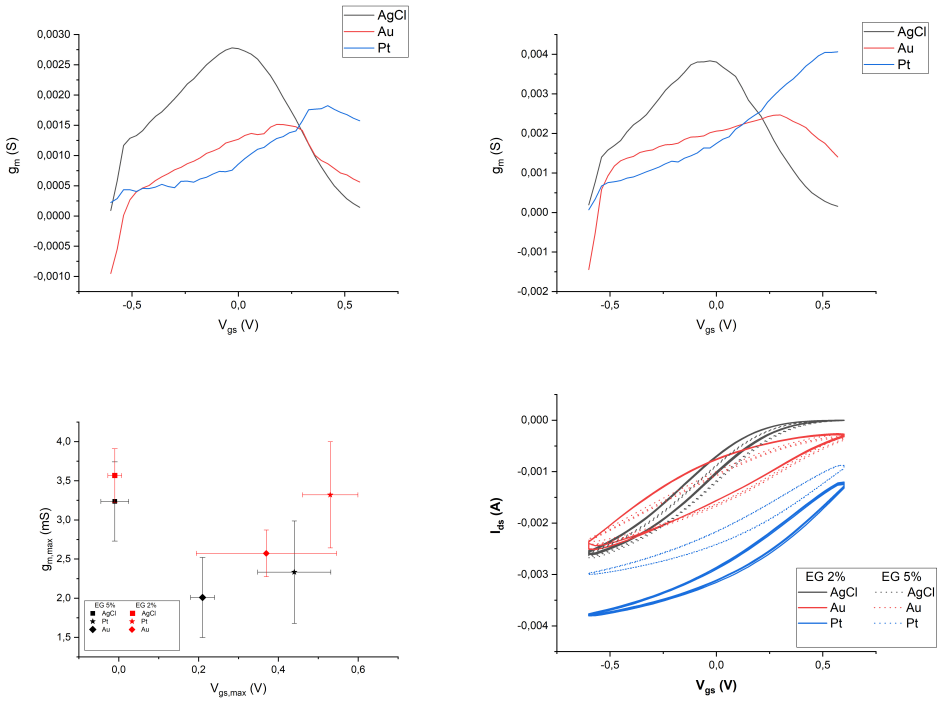

Figure 4.6: Transconductances comparison with different gates of 5% EG device (on top-left) and 2% EG device (on top-right). Maximum transconductances ink comparison obtained with different gates (on bottom-left). Transcharacteristics ink comprison obtained with different gates (on bottom-right). These four graphs focus on the two better configurations: EG 2% and EG 5%.

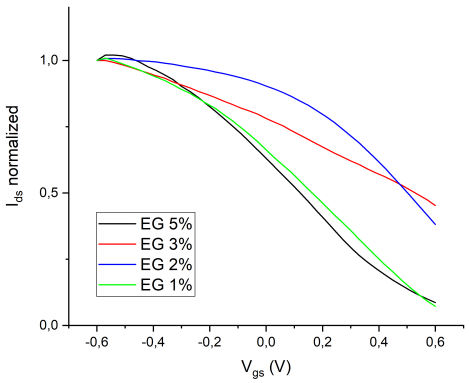

Figure 4.7: Normalized I_{DS} ink comparison obtained with Au gate. Normalized I_{DS} is equal to $I_{DS} = (I_{V_{GS}=0.6V} - I_{V_{GS}=-0.6V})/I_{V_{GS}=-0.6V}$

At the end of measurement analysis, the configuration that appears to offer the most promising results is the one with an EG concentration of 2% (see the table above), since it has a good current modulation and the highest transconductance peak value.
Once the ink formulation had been selected, the deposition techniques were investigated in order to identify the most suitable one, using the gold gate.

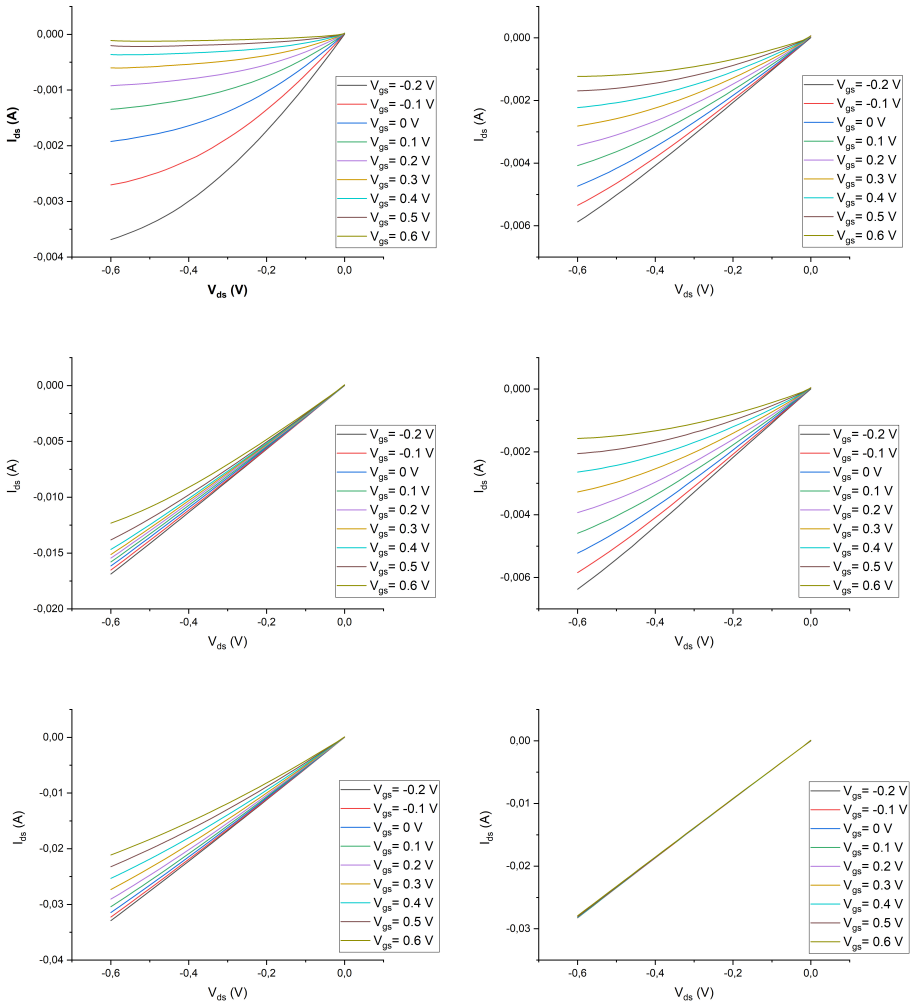

Figure 4.8: Output characteristics for different deposition techniques: inkjet single layer on top-left, inkjet double layer with spacing of 80 μm on top right, inkjet double layer with spacing of 50 μm on middle-left, inkjet double layer with spacing of 50 μm (with a shrinked print pattern) on middle-right, aerosol jet double layer on bottom left, spin coating (multi-layer) on bottom-right.

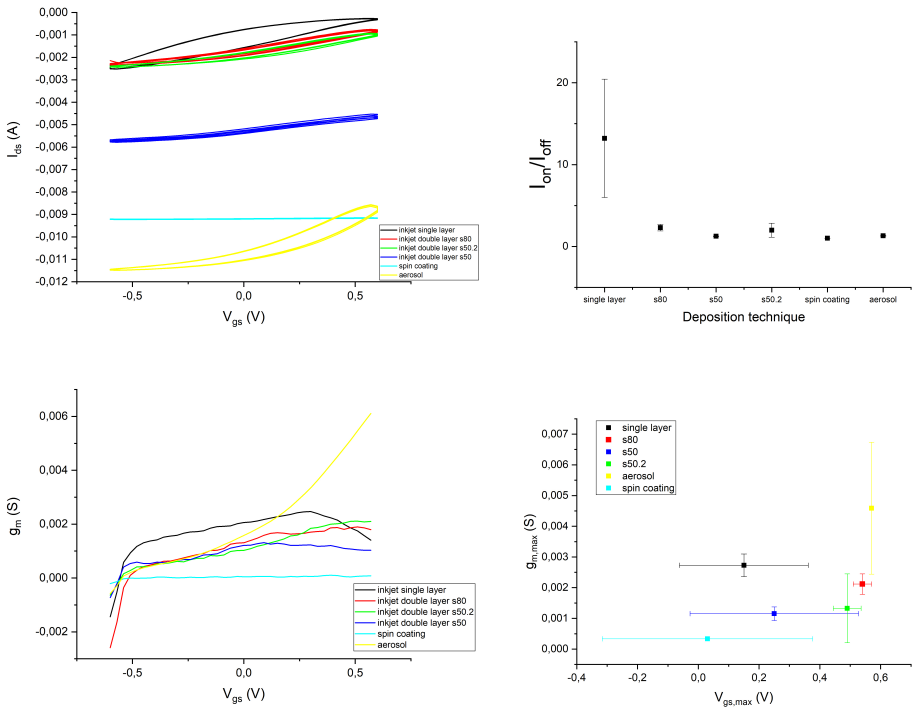

Figure 4.9: Transcharacteristics deposition techniques comparison (on top-left). I_{on}/I_{off} deposition techniques comparison (on top-right). Transconductances deposition techniques comparison (on bottom-left). Maximum transconductances deposition techniques comparison (on bottom-right).

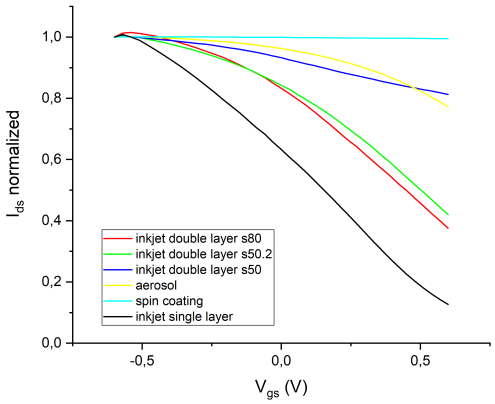

Figure 4.10: Normalized I_{DS} deposition techniques comparison obtained with Au gate. Normalized I_{DS} is equal to $I_{DS} = (I_{V_{GS}=0.6V} - I_{V_{GS}=-0.6V})/I_{V_{GS}=-0.6V}$

At the end of the measurement analysis, it was observed that better results are obtained in the inkjet single layer case, establishing that inkjet printing is the most stable deposition technique, exhibiting superior characteristics. In fact, in the previous graphs, it is possible to observe that inkjet single layer devices have the best current modulation ($\sim 75\%$), the highest I_{on}/I_{off} ratio, and one of the highest and closest to 0 V maximum transcondutance value (its position is proportional to the film thickness).
The nozzle diameter affects the volume and the velocity of the ejected droplets; in fact, the smallest nozzle is used to increase the resolution in the case of fine structure, while a larger one reduces the frequency of clogging events. The following table illustrates the mean thickness of the printed devices measured through the profilometer; it is evident that the devices printed with a spacing parameter of 50 μm are thicker than those printed with a spacing of 80 μm, as expected.

Deposited PEDOT:PSS thickness		
Spacing	50 μm	80 μm
Device 1	305 nm	256 nm
Device 2	285 nm	273 nm
Device 3	333 nm	268 nm
Device 4	361 nm	273 nm
Device 5	339 nm	270 nm
Device 6	312 nm	261 nm
Mean	323 nm	267 nm

Measurements on the final optimized devices are conducted after the fabrication and again after ten days, in order to check the stability of the devices.

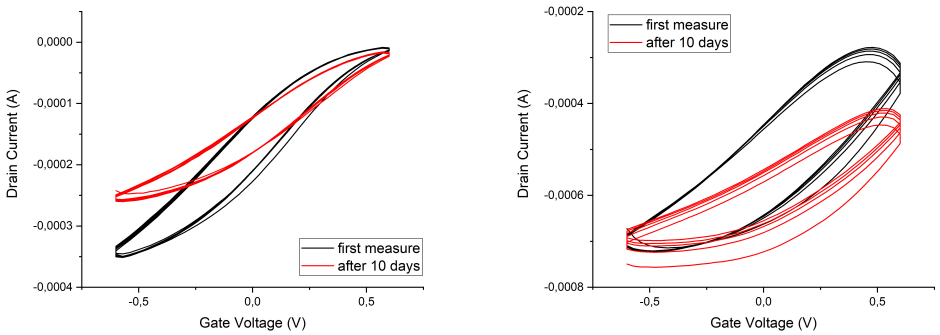

Figure 4.11: Transcharacteristic of devices printed with nozzle of 50 μm on the left and 80 μm on the right.

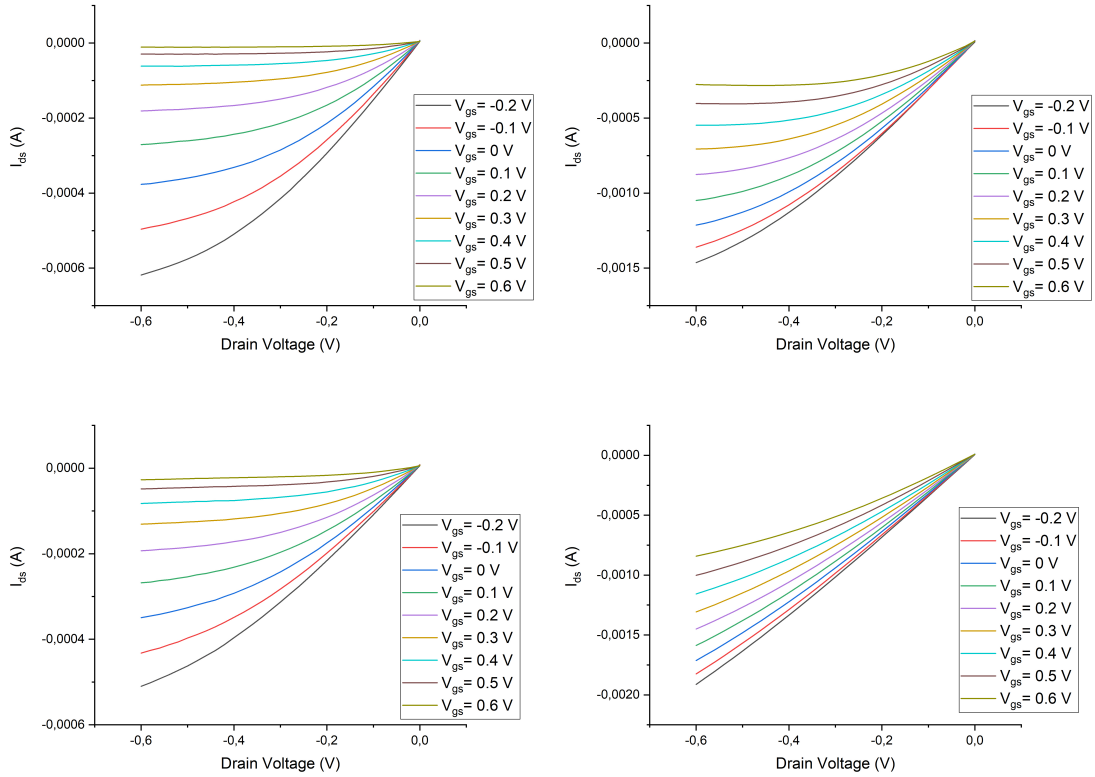

Figure 4.12: Output characteristic of devices printed with nozzle of 50 μm on the left and 80 μm on the right: top figures refers to first measurement, while bottom figures refers to measurements after 10 days.

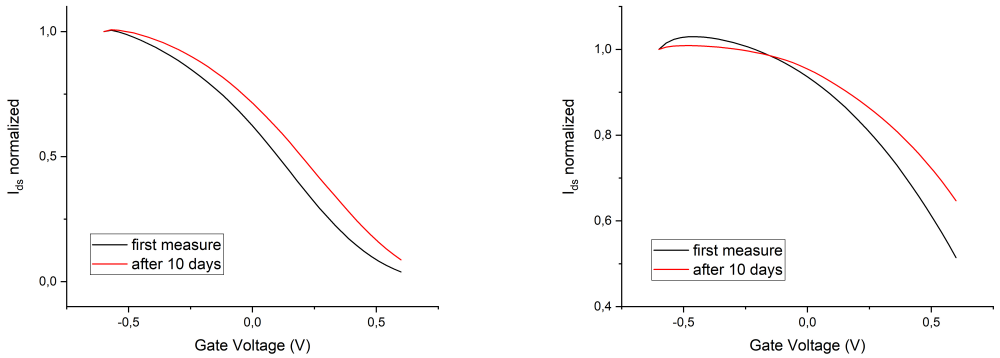

Figure 4.13: Normalized I_{DS} of devices printed with nozzle of 50 μm on the left and 80 μm on the right.

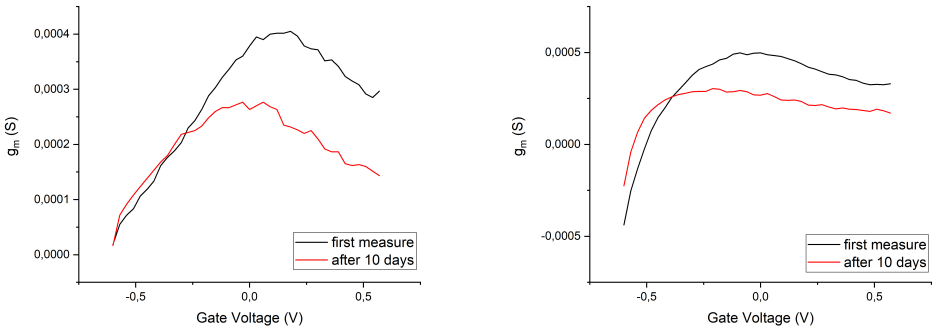

Figure 4.14: Transconductance of devices printed with nozzle of 50 μm on the left and 80 μm on the right.

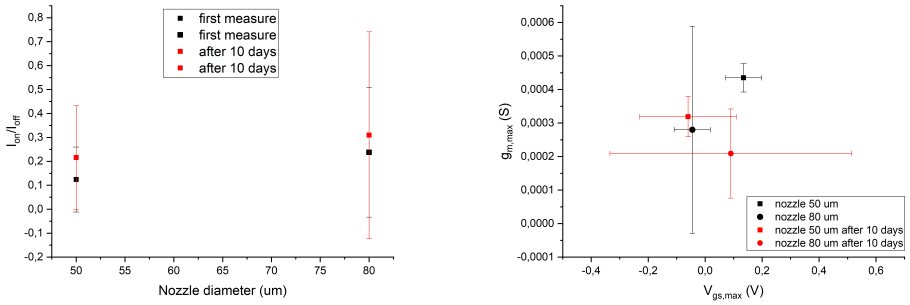

Figure 4.15: I_{on}/I_{off} comparison on the left and maximum transconductances comparison on the right.

The graphs above demonstrate that measurements taken 10 days after the initial ones exhibit lower values, as expected. However, the observed variation is minimal, indicating that the devices exhibit a high degree of stability in their characteristics over time.

4.3 BPS test

In order to verify the correct behaviour of the BPS microfluidic, a preliminary test with blue dye is performed. For this test, the PDMS layer is bonded on a non-etched glass, allowing the dye, injected through a micro-pipette in the inlet, to flow towards provisional outlets (not present in the final device) that are opened at the end of each branch, as shown in figure 4.16.

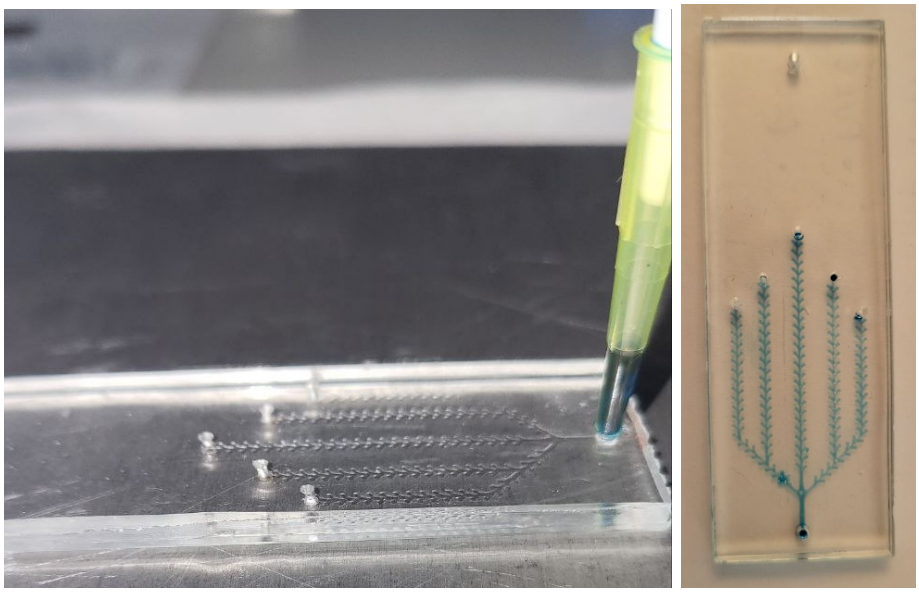

Figure 4.16: Dye test

Regarding the etched glass, to ensure that the etching depth is within the correct range, profilometer analysis is accomplished, as illustrated by the following chart. The mean value obtained by measuring six different etched-glasses is 1.1 μm.

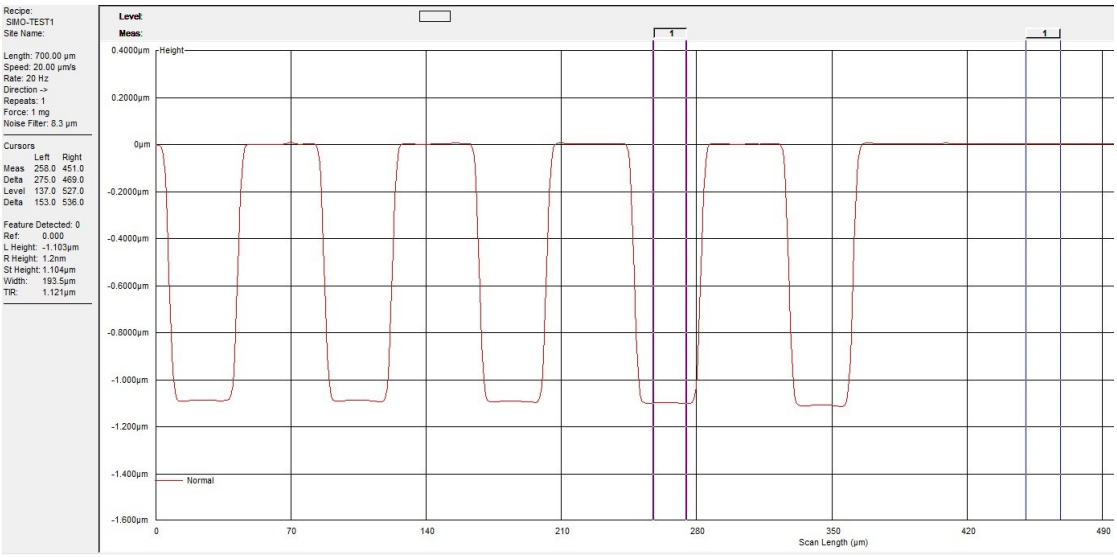

Figure 4.17: Profilometer example measurement of etched glass

At this point, plasma bonding is performed and then flow tests are conducted again, employing initially ethanol, which facilitates the wetting of the PDMS more

effectively than water, followed by test with blue dye, shown in the left image of figure 4.18. These tests show a difficult fluid flow in the etched glass, probably due to the reduced thickness of the etched channels or the high number of pillars contained within them.

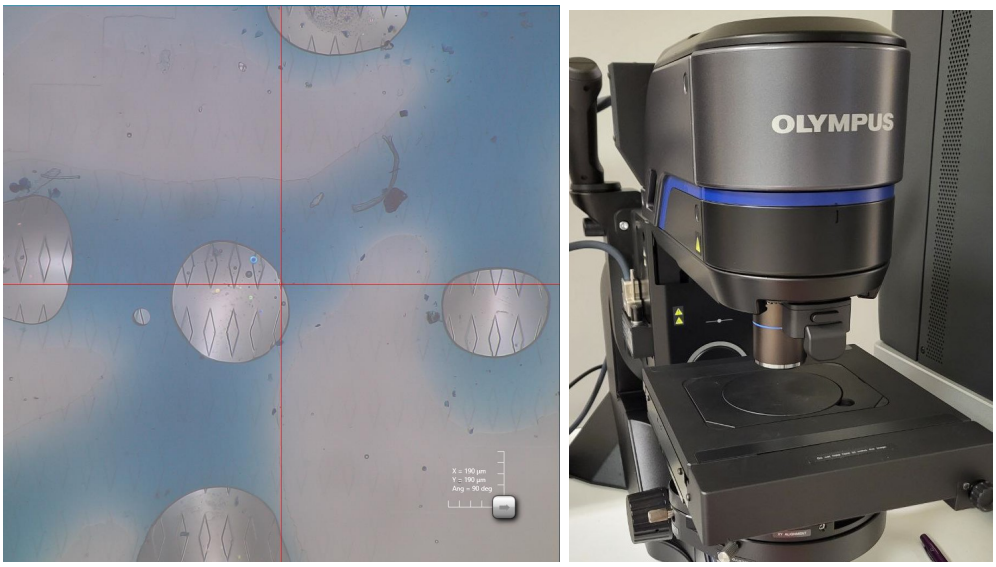

Figure 4.18: BPS blue dye test on the left: air bubbles can be observed in the channel. This image and also printed device images are taken by Olympus microscope shown in the image on the right.

Chapter 5

Conclusions and Perspectives

The focus of this thesis is the fabrication of a microfluidic platform which integrates an OECT that can be employed in the detection of cardiac biomarkers by analysing pure plasma extracted by a blood/plasma separator.
Regarding the OECT, the main aspects that have been analysed are:

- identifying the optimal printing ink and its formulation;
- determining the most effective printing deposition technique between spin coating, aerosol jet printer and inkjet printer, optimizing also the printing parameters.

The implementation of these enhancements has led to the achievement of a satisfactory degree of stability and current modulation, fundamental aspects for the biosensing application; in fact, these parameters affect the detection sensitivity during biosensing measurements.
It is of paramount importance to achieve a stable platform over time in order to maintain the precision during biomarker detection. Furthermore, it is crucial to achieve higher sensitivity in order to detect biomarkers in lower concentrations, thus enabling the early detection of an infarction in the case of cardiac troponin (cTnI) and C-reactive protein detection.
With regard to potential enhancements, it would be beneficial to explore the possibility of modifying the geometry (W, L, d) of the OECT, since it affects the response time and the transconductance value with the corresponding V_{GS}. In fact, thickness film increase corresponds to an increase of $g_{m,max}$ and $V_{GS,max}$, but also to an increase of response time, so a trade-off could be beneficial. In addition, minimizing $V_{GS,max}$ is beneficial for biosensing application, since biorecognition elements can be sensitive to prolonged application of a bias [22].

For this reason, investigating other $\frac{W}{L}$ ratio, such as 0.6, 1, 2, 10, instead of the actual $\frac{W}{L} = 30$, could bring improvements.
Additional PEDOT-ink print optimizations could be sought in order to enhance the device switch-off, utilizing the favourable outcomes achieved as a starting point.
Concerning the blood/plasma separator, the tests carried out on the final device demonstrate a high resistance to fluid flow in the plasma compartment (etched glass side), preventing the fluid from reaching the outlet (responsible for future plasma collection). One potential solution could be to extend the etching times in order to create deeper collection channels (for example, from 90 seconds to 120-150 seconds), thereby approaching the 2 μm depth limit (which is necessary to trap the red blood cells) as closely as possible.
Once both the preparation and the sensing platforms will be optimized, their integration is required. Then, functional tests with real samples (whole blood) are foreseen.

Bibliography

[1] Dion Khodagholy et al. «High transconductance organic electrochemical transistors». In: *Nature Communications* 4 (2013), pp. 1–6. ISSN: 20411723. DOI: 10.1038/ncomms3133 (cit. on p. 2).

[2] Marios Sophocleous, Laura Contat-Rodrigo, Eduardo Garcia-Breijo, and Julius Georgiou. «Organic electrochemical transistors as an emerging platform for bio-sensing applications: A review». In: *IEEE Sensors Journal* 21.4 (2021), pp. 3977–4006. ISSN: 15581748. DOI: 10.1109/JSEN.2020.3033283 (cit. on pp. 2, 11, 19).

[3] Yue Niu, Ze Qin, Ying Zhang, Chao Chen, Sha Liu, and Hu Chen. «Expanding the potential of biosensors: a review on organic field effect transistor (OFET) and organic electrochemical transistor (OECT) biosensors». In: *Materials Futures* 2.4 (2023). ISSN: 27525724. DOI: 10.1088/2752-5724/ace3dd (cit. on pp. 2, 11, 19).

[4] Buddhadev Purohit, Pramod R. Vernekar, Nagaraj P. Shetti, and Pranjal Chandra. «Biosensor nanoengineering: Design, operation, and implementation for biomolecular analysis». In: *Sensors International* 1.July (2020), p. 100040. ISSN: 26663511. DOI: 10.1016/j.sintl.2020.100040. URL: https://doi.org/10.1016/j.sintl.2020.100040 (cit. on pp. 3, 7).

[5] Carlo Ricciardi. *Nanobiosensors (Physics of NanoBiosystems)* (cit. on pp. 4, 7, 8).

[6] Junfei Wang, Zhenyu Xu, and Domna G. Kotsifaki. «Plasmonic and metamaterial biosensors: a game-changer for virus detection». In: *Sensors and Diagnostics* 2.3 (2023), pp. 600–619. ISSN: 26350998. DOI: 10.1039/d2sd00217e. arXiv: 2212.05636 (cit. on p. 5).

[7] Matteo Cocuzza. *Biosensors (Advanced Technologies and Applications)* (cit. on p. 6).

[8] Tanu Bhardwaj. «Review on Biosensor Technologies». In: *International Journal of Advanced Research in Engineering and Technology* 6.2 (2015), pp. 36–62. URL: www.jifactor.com (cit. on p. 6).

[9] «Sensing Inflammation Biomarkers with Electrolyte-Gated Organic Electronic Transistors». In: *Advanced Healthcare Materials* 10.20 (2021). ISSN: 21922659. DOI: 10.1002/adhm.202100955 (cit. on pp. 6, 8, 12).

[10] Valentina Preziosi, Mario Barra, Giovanna Tomaiuolo, Pasquale D'Angelo, Simone Luigi Marasso, Alessio Verna, Matteo Cocuzza, Antonio Cassinese, and Stefano Guido. «Organic electrochemical transistors as novel biosensing platforms to study the electrical response of whole blood and plasma». In: *Journal of Materials Chemistry B* 10.1 (2022), pp. 87–95. ISSN: 20507518. DOI: 10.1039/d1tb01584b (cit. on p. 8).

[11] Aiguo Wu and Waheed S. Khan. *Nanobiosensors: From design to applications*. 2020, pp. 1–398. ISBN: 9783527345137. DOI: 10.1002/9783527345137 (cit. on p. 8).

[12] W. S. Mielczarek, E. A. Obaje, T. T. Bachmann, and M. Kersaudy-Kerhoas. «Microfluidic blood plasma separation for medical diagnostics: Is it worth it?» In: *Lab on a Chip* 16.18 (2016), pp. 3441–3448. ISSN: 14730189. DOI: 10.1039/c6lc00833j (cit. on p. 9).

[13] LIFEBLOOD. «A lab-on-a-chip integrated with electrochemical transistors for cardiac biomarkers evaluation in human blood». In: () (cit. on p. 9).

[14] Jonathan Rivnay, Sahika Inal, Alberto Salleo, Róisín M. Owens, Magnus Berggren, and George G. Malliaras. «Organic electrochemical transistors». In: *Nature Reviews Materials* 3 (2018). ISSN: 20588437. DOI: 10.1038/natrevmats.2017.86 (cit. on pp. 10, 12, 14, 15, 18).

[15] Anna Köhler and Bässler Heinz. *Electronic Processes in Organic Semiconductors*. ISBN: 9783527410538 (cit. on pp. 10, 20, 22).

[16] Jacob T. Friedlein, Robert R. McLeod, and Jonathan Rivnay. «Device physics of organic electrochemical transistors». In: *Organic Electronics* 63.June (2018), pp. 398–414. ISSN: 15661199. DOI: 10.1016/j.orgel.2018.09.010 (cit. on p. 10).

[17] «Organic Bioelectronics Development in Italy: A Review». In: *Micromachines* 14.2 (2023). ISSN: 2072666X. DOI: 10.3390/mi14020460 (cit. on pp. 11, 12, 19, 34).

[18] Daniel A. Bernards and George G. Malliaras. «Steady-state and transient behavior of organic electrochemical transistors». In: *Advanced Functional Materials* 17.17 (2007), pp. 3538–3544. ISSN: 1616301X. DOI: 10.1002/adfm.200601239 (cit. on pp. 13, 15, 18).

[19] David Ohayon, Victor Druet, and Sahika Inal. «A guide for the characterization of organic electrochemical transistors and channel materials». In: *Chemical Society Reviews* 52.3 (2023), pp. 1001–1023. ISSN: 14604744. DOI: 10.1039/d2cs00920j (cit. on pp. 13, 16, 17, 19).

[20] Antonio Facchetti. «Semiconductors for organic transistors». In: *Materials Today* 10.3 (2007), pp. 28–37. ISSN: 13697021. DOI: 10.1016/S1369-7021(07)70017-2. URL: http://dx.doi.org/10.1016/S1369-7021(07)70017-2 (cit. on p. 14).

[21] «Rapid prototyping of 3D Organic Electrochemical Transistors by composite photocurable resin». In: *Scientific Reports* 10.1 (2020), pp. 1–11. ISSN: 20452322. DOI: 10.1038/s41598-020-70365-8. URL: https://doi.org/10.1038/s41598-020-70365-8 (cit. on p. 17).

[22] Jonathan Rivnay, Pierre Leleux, Michele Sessolo, Dion Khodagholy, Thierry Hervé, Michel Fiocchi, and George G. Malliaras. «Organic electrochemical transistors with maximum transconductance at zero gate bias». In: *Advanced Materials* 25.48 (2013), pp. 7010–7014. ISSN: 09359648. DOI: 10.1002/adma.201303080 (cit. on pp. 18, 66).

[23] Simonetta Klein. «Legami, formule e geometrie molecolari». In: *Il racconto della chimica*. 2018. Chap. 11, pp. 53–54 (cit. on p. 21).

[24] «A short review article on conjugated polymers». In: *Journal of Polymer Research* 30.3 (2023), pp. 1–15. ISSN: 15728935. DOI: 10.1007/s10965-023-03451-w. URL: https://doi.org/10.1007/s10965-023-03451-w (cit. on p. 21).

[25] Zeng Fan and Jianyong Ouyang. «Thermoelectric Properties of PEDOT:PSS». In: *Advanced Electronic Materials* 5.11 (2019), pp. 1–23. ISSN: 2199160X. DOI: 10.1002/aelm.201800769 (cit. on p. 21).

[26] Anton V. Volkov et al. «Understanding the Capacitance of PEDOT:PSS». In: *Advanced Functional Materials* 27.28 (2017), pp. 1–10. ISSN: 16163028. DOI: 10.1002/adfm.201700329 (cit. on p. 21).

[27] Manfred Scholdt, Hung Do, Johannes Lang, Andre Gall, Alexander Colsmann, Uli Lemmer, Jan D. Koenig, Markus Winkler, and Harald Boettner. «Organic semiconductors for thermoelectric applications». In: *Journal of Electronic Materials* 39.9 (2010), pp. 1589–1592. ISSN: 03615235. DOI: 10.1007/s11664-010-1271-8 (cit. on p. 21).

[28] Sophia L. Bidinger, Sanggil Han, George G. Malliaras, and Tawfique Hasan. «Highly stable PEDOT:PSS electrochemical transistors». In: *Applied Physics Letters* 120.7 (2022). ISSN: 00036951. DOI: 10.1063/5.0079011 (cit. on pp. 22, 55).

[29] «PEDOT:PSS organic electrochemical transistor arrays for extracellular electrophysiological sensing of cardiac cells». In: *Biosensors and Bioelectronics* 93.June 2016 (2017), pp. 132–138. ISSN: 18734235. DOI: 10.1016/j.bios.2016.09.047. URL: http://dx.doi.org/10.1016/j.bios.2016.09.047 (cit. on pp. 22, 23).

[30] Yuanying Liang, Andreas Offenhäusser, Sven Ingebrandt, and Dirk Mayer. «PEDOT:PSS-Based Bioelectronic Devices for Recording and Modulation of Electrophysiological and Biochemical Cell Signals». In: *Advanced Healthcare Materials* 10.11 (2021). ISSN: 21922659. DOI: 10.1002/adhm.202100061 (cit. on p. 22).

[31] Stratasys. *Stampante 3D Objet30*. URL: https://www.stratasys.com/it/3d-printers/printer-catalog/objet30-printer/ (cit. on p. 27).

[32] Alvaro Mata, Aaron J. Fleischman, and Shuvo Roy. «Characterization of Polydimethylsiloxane (PDMS) Properties for Biomedical Micro/Nanosystems». In: *Biomedical Microdevices* 7.4 (2005), pp. 281–293. ISSN: 15728781. DOI: 10.1007/s10544-005-6070-2 (cit. on p. 27).

[33] Inês Miranda, Andrews Souza, Paulo Sousa, João Ribeiro, Elisabete M.S. Castanheira, Rui Lima, and Graça Minas. «Properties and applications of PDMS for biomedical engineering: A review». In: *Journal of Functional Biomaterials* 13.1 (2022). ISSN: 20794983. DOI: 10.3390/jfb13010002 (cit. on pp. 27–29).

[34] Say Hwa Tan, Nam Trung Nguyen, Yong Chin Chua, and Tae Goo Kang. «Oxygen plasma treatment for reducing hydrophobicity of a sealed polydimethylsiloxane microchannel». In: *Biomicrofluidics* 4.3 (2010), pp. 1–8. ISSN: 19321058. DOI: 10.1063/1.3466882 (cit. on p. 28).

[35] Marc P. Wolf, Georgette B. Salieb-Beugelaar, and Patrick Hunziker. «PDMS with designer functionalities—Properties, modifications strategies, and applications». In: *Progress in Polymer Science* 83 (2018), pp. 97–134. ISSN: 00796700. DOI: 10.1016/j.progpolymsci.2018.06.001. URL: https://doi.org/10.1016/j.progpolymsci.2018.06.001 (cit. on p. 28).

[36] Bastien Venzac, Shanliang Deng, Ziad Mahmoud, Aufried Lenferink, Aurélie Costa, Fabrice Bray, Cees Otto, Christian Rolando, and Séverine Le Gac. «PDMS Curing Inhibition on 3D-Printed Molds: Why? Also, How to Avoid It?» In: *Analytical Chemistry* 93.19 (2021), pp. 7180–7187. ISSN: 15206882. DOI: 10.1021/acs.analchem.0c04944 (cit. on p. 29).

[37] Wikipedia. *Photoresist*. URL: https://en.wikipedia.org/wiki/Photoresist (cit. on p. 32).

[38] Ossila. *Spin coating*. URL: https://www.ossila.com/pages/solution-processing-techniques-comparison (cit. on p. 34).

[39] L. Jay Deiner and Thomas L. Reitz. «Inkjet and Aerosol Jet Printing of Electrochemical Devices for Energy Conversion and Storage». In: *Advanced Engineering Materials* 19.7 (2017), pp. 1–18. ISSN: 15272648. DOI: 10.1002/adem.201600878 (cit. on pp. 35, 42, 43).

[40] N. J. Wilkinson, M. A.A. Smith, R. W. Kay, and R. A. Harris. «A review of aerosol jet printing—a non-traditional hybrid process for micro-manufacturing». In: *International Journal of Advanced Manufacturing Technology* 105.11 (2019), pp. 4599–4619. ISSN: 14333015. DOI: 10.1007/s00170-019-03438-2 (cit. on pp. 35, 42).

[41] Ana Moya, Gemma Gabriel, Rosa Villa, and F. Javier del Campo. «Inkjet-printed electrochemical sensors». In: *Current Opinion in Electrochemistry* 3.1 (2017), pp. 29–39. ISSN: 24519111. DOI: 10.1016/j.coelec.2017.05.003. URL: https://doi.org/10.1016/j.coelec.2017.05.003 (cit. on pp. 35, 36).

[42] Saleem Khan, Shawkat Ali, and Amine Bermak. «Smart Manufacturing Technologies for Printed Electronics». In: *Hybrid Nanomaterials*. Ed. by Rafael Vargas-Bernal, Peng He, and Shuye Zhang. Rijeka: IntechOpen, 2019. Chap. 7. DOI: 10.5772/intechopen.89377. URL: https://doi.org/10.5772/intechopen.89377 (cit. on p. 36).

[43] Madhusudan Singh, Hanna M. Haverinen, Parul Dhagat, and Ghassan E. Jabbour. «Inkjet printing-process and its applications». In: *Advanced Materials* 22.6 (2010), pp. 673–685. ISSN: 09359648. DOI: 10.1002/adma.200901141 (cit. on p. 36).

[44] Seongju Kim, Minsu Cho, and Sungjune Jung. «The design of an inkjet drive waveform using machine learning». In: *Scientific Reports* 12.1 (2022), pp. 1–10. ISSN: 20452322. DOI: 10.1038/s41598-022-08784-y. URL: https://doi.org/10.1038/s41598-022-08784-y (cit. on p. 36).

[45] Cheng Han Wu and Weng Sing Hwang. «The effect of the echo-time of a bipolar pulse waveform on molten metallic droplet formation by squeeze mode piezoelectric inkjet printing». In: *Microelectronics Reliability* 55.3-4 (2015), pp. 630–636. ISSN: 00262714. DOI: 10.1016/j.microrel.2014.11.014. URL: http://dx.doi.org/10.1016/j.microrel.2014.11.014 (cit. on p. 39).

[46] Dwipayan Patnaik Vivek Subramanian and Ed Sayeef Salahuddin. «Three-Dimensional Structure Formation via Inkjet-printed Metal Nanoparticles: Ink and Application Development». In: (2018). URL: http://www2.eecs.berkeley.edu/Pubs/TechRpts/2018/EECS-2018-96.html (cit. on p. 39).

[47] Zhaoting Xiong and Changqing Liu. «Optimization of inkjet printed PEDOT:PSS thin films through annealing processes». In: *Organic Electronics* 13.9 (2012), pp. 1532–1540. ISSN: 15661199. DOI: 10.1016/j.orgel.2012.05.005. URL: http://dx.doi.org/10.1016/j.orgel.2012.05.005 (cit. on p. 41).

[48] Ethan B. Secor. «Principles of aerosol jet printing». In: *Flexible and Printed Electronics* 3.3 (2018). ISSN: 20588585. DOI: 10.1088/2058-8585/aace28 (cit. on pp. 42, 43).

[49] Pasquale D'Angelo et al. «Homocysteine solution-induced response in aerosol jet printed oects by means of gold and platinum gate electrodes». In: *International Journal of Molecular Sciences* 22.21 (2021), pp. 1–14. ISSN: 14220067. DOI: 10.3390/ijms222111507 (cit. on p. 43).

[50] AUSTRALIA SURFACE METROLOGY LAB. *Stylus Profilometry*. URL: https://australiasurfacemetrologylab.org/new-page (cit. on p. 44).

[51] Keysight. *SMU*. URL: https://www.keysight.com/zz/en/product/B2912A/precision-source-measure-unit-2-ch-10fa-210v-3a-dc-10-5a-pulse.html (cit. on p. 44).

[52] Shadi Karimi, Pouya Mehrdel, Josep Farré-Lladós, and Jasmina Casals-Terré. «A passive portable microfluidic blood-plasma separator for simultaneous determination of direct and indirect ABO/Rh blood typing». In: *Lab on a Chip* 19.19 (2019), pp. 3249–3260. ISSN: 14730189. DOI: 10.1039/c9lc00690g (cit. on pp. 50, 51).